THESIS FOR THE DEGREE OF DOCTOR OF PHILOSOPHY

High Performance Cooling of Traction Brushless Machines

ALESSANDRO ACQUAVIVA

Department of Electrical Engineering
Division of Electric Power Engineering
CHALMERS UNIVERSITY OF TECHNOLOGY
Gothenburg, Sweden 2021

High Performance Cooling of Traction Brushless Machines
ALESSANDRO ACQUAVIVA
ISBN 978-91-7905-433-5

Doktorsavhandlingar vid Chalmers Tekniska Högskola
Ny serie nr. 4900
ISSN 0346-718X

Department of Electrical Engineering
Division of Electric Power Engineering
Chalmers University of Technology
SE–412 96 Göteborg
Sweden
Telephone +46 (0)735704363

Chalmers Bibliotek, Reproservice
Gothenburg, Sweden 2021

To those who inspired and supported me over the years.

High Performance Cooling of Traction Brushless Machines
ALESSANDRO ACQUAVIVA
Department of Electrical Engineering
Chalmers University of Technology

Abstract

The work presented in this thesis covers several aspects of traction electric drive system design. Particular attention is given to the traction electrical machine with focus on the cooling solution, thermal modelling and testing.

A 60 kW peak power traction machine is designed to achieve high power density and high efficiency thanks to direct oil cooling. The machine selected has a tooth coil winding, also defined as non-overlapping fractional slot concentrated winding. This winding concept is state of the art for many applications with high volumes and powers below 10 kW. Also, these have been proven successful in high power applications such as wind power generators. In this thesis, it is shown that this technology is promising also for traction machines and, with some suggested design solutions, can present certain unique advantages when it comes to manufacturing and cooling.

The traction machine in this work is designed for a small two-seater electric vehicle but could as well be used in a parallel hybrid. The proposed solution has the advantage of having a simple winding design and of integrating the cooling within the stator slot and core. A prototype of the machine has been built and tested, showing that the machine can operate with current densities of up to 35 A/mm^2 for 30 seconds and 25 A/mm^2 continuously. This results in a net power density of the built prototype of 24 kW/l and a gross power density of 8 kW/l with a peak efficiency above 94%. It is shown that a version of the same design optimized for mass manufacturing has the potential of having a gross power density of 15.5 kW/l which would be comparable with the best in class traction machines found on the automotive industry.

The cooling solution proposed is resulting in significantly lower winding temperature and an efficiency gain between 1.5% and 3.5% points, depending on the drivecycle, compared to an external jacket cooling, which is a common solution for traction motors.

Index Terms: Cooling, energy efficiency, electrical machine design, permanent

magnet synchronous machine (PMSM), drivetrain system analysis.

Acknowledgements

First and foremost, I would like to express my gratitude to my main supervisor Prof. Sonja Lundmark and my examiner Prof. Torbjörn Thiringer for their great support, guidance and mentoring. I would also like to thank my co-supervisor Dr. Emma Grunditz for her valuable time, kindness and contribution. I really enjoyed working with all of you.

A special thanks to Dr. Stefan Skoog for sharing the daily challenges and for the very fruitful collaboration. I am grateful also to all the other colleagues and friends at Electric Power Engineering for creating such a great work environment.

I had the chance and pleasure to spend some time at KTH with Prof. Wallmark and at Politecnico di Torino with Prof. Guglielmi, these experiences enriched my knowledge and my experience as a researcher.

Finally, I would like to thank my family for unconditional love and always supporting my choices no matter how far from home I get. I am infinitely grateful to my dad for inspiring and challenging me as a kid and over the years.

I gratefully acknowledge The Swedish Energy Agency for the financial support.

Alessandro Acquaviva
Gothenburg, Sweden
February, 2021

Contents

Abstract **v**

Acknowledgements **vii**

Contents **ix**

List of Symbols **1**

1 Introduction **3**
1.1 Problem background 3
1.2 Technological background 5
1.3 Review of previous work 8
1.4 Purpose of the thesis and contributions 9
1.5 Thesis outline 11
1.6 List of publications 12

2 Electrical machines state of the art and modelling **15**
2.1 Traction electrical machines state of the art 15
2.1.1 Tooth coil winding machine 17
2.2 Permanent magnet synchronous machine electromagnetic model . . 20
2.3 Cooling of traction electric motors and drive-trains 21
2.4 Thermal modelling of electrical machines 22
2.4.1 Lumped-parameter network - thermal parameters 23
2.5 The calorimetric measurement method 24

3 Design of the tooth coil winding traction PM machine **27**
3.1 Vehicle description and design specifications 27
3.2 Machine design 29

3.2.1 Electromagnetic Design 30
3.2.2 Thermal design and cooling 40
3.3 Design improvements for production version 43

4 Test set-ups and measurements **45**
4.1 Set-up 1 - Main investigated machine with closed loop oil-to-water circuit 45
4.2 Set-up 2 - Electrical machine open loop water circuit 50
4.3 Set-up 3 - Power converter open loop water circuit 53

5 Electric drivetrain thermal modelling and analysis **55**
5.1 System modelling 55
5.2 System analysis 58
5.3 Comparison - water/glycol cooling jacket vs direct oil cooling . . . 62

6 Conclusions and future work **67**

Bibliography **71**
References 71

Appendices **76**

A Assumptions and derivations for Table 1.1 **77**

B LP network derivations **81**
B.1 Direct cooling machine LP 81
B.2 Cooling jacket machine LP 83

List of Symbols

j	imaginary unit	-
d	differential operator	-
v	voltage	[V]
i	current	[A]
R	resistance	[Ω]
L	inductance	[H]
l	incremental inductance	[H]
Ψ	flux linkage	[Wb]
p	number of poles	-
ω	electrical angular frequency	[rad/s]
n	mechanical angular speed	[rpm]
ξ	saliency	-
C_{th}	thermal capacitance	[J/K]
R_{th}	thermal resistance	[K/W]
T	torque	[Nm]
Θ	temperature	[K]
V	volume	[m^3]
$\dot{V}$	volumetric flow rate	[m^3/s]
A	area	[m^2]
r	radius	[m]
θ	mechanical angle	[rad]
ρ_{m}	specific mass	[$\mathrm{kg/m}^3$]
C_{p}	specific heat	[J/(kg K)]
λ	thermal conductivity	[W/(m K)]
h	convection heat transfer coefficient	[W/(m^2 K)]

μ_r	relative permeability	-
μ_0	permeability of vacuum	[H/m]
ρ	resistivity	[Ωm]

Introduction

1.1 Problem background

One of the challenges of the twenty-first century is fighting climate change. Environmental research highlights how there is an increase in the average Earth temperature, which is significantly faster than temperature swings registered in the past, and the trend is not promising. According to scientists in the field, a raise of 2°C would cause a significant and irreversible climate impact. Glacier melting and an raising sea level are just part of the possible consequences. Research has correlated the temperature increase with the greenhouse gas emission increase. Another aspect is that city pollution is a concern for health and quality of life.

Passenger vehicles are responsible for around 12% (data from 2014) of total EU emissions of carbon dioxide (CO_2), the main greenhouse gas. If vans and heavy duty vehicles are included the number rises above 20% [1]. The transportation impact on the greenhouse gas emission is significant, as can be seen in Fig. 1.1.

With these premises, and assuming that at the source there is a shift to renewable energy, a move towards a sustainable transportation is a clear need to avoid climate change. The trend is positive, in fact, the market for electric vehicles (EV) is strong, with an annual market growth rate above 40% year-on-year from 2010 [3].

As of today, the biggest technological challenges in the EV industry, are related to the energy storage and charging infrastructure. However, the electric drivetrain efficiency, compactness and cost play a very important role in the development of the future generation of EVs. In a few years from now, traction electric drivetrains will be produced with the rate of millions per year [3]. Ensuring

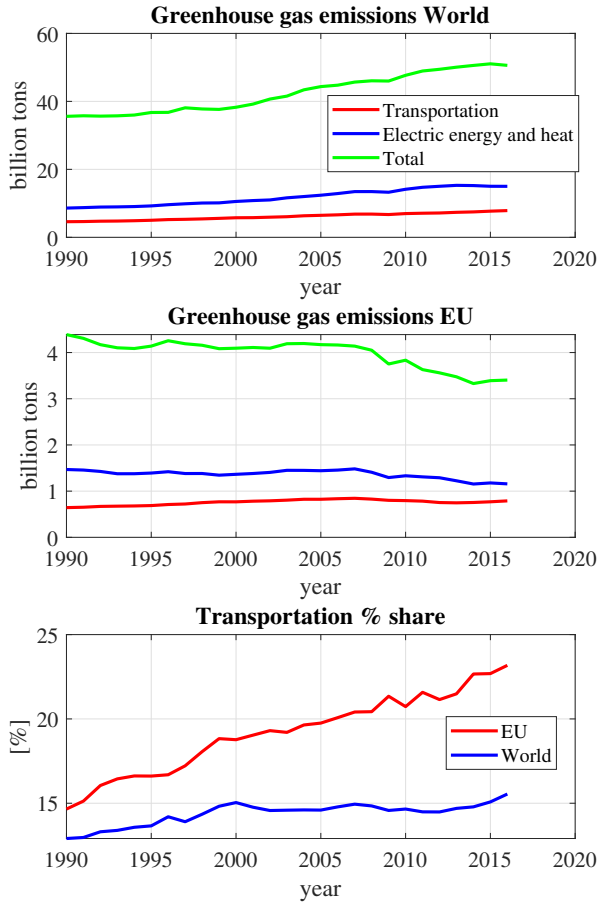

Figure 1.1: Greenhouse gas emissions in the World and in EU. Greenhouse gas emissions are measured in tonnes of carbon dioxide-equivalents (CO_2e) [2].

a simple, effective and reliable manufacturing process of both the power converters and traction electrical machines is the key to succeed in the electric vehicle industry. It took many years to reach the current quality for the manufacturing process of the internal combustion engine. However, a much faster development is needed for the electric drive-train if the sustainability goals, set for 2030, about CO_2 emissions are to be met. EU aims at reducing the net human-caused emissions of carbon dioxide (CO2) by at least 55 percent from the 2010 levels by 2030, reaching

'net zero' around 2050 [1].

1.2 Technological background

The industry trend is to move towards highly integrated drivetrains, where often the electric machine and the power electronics share the same cooling loop, aiming at high power density, high efficiency and low cost.

Semiconductor technology development is one of the factors that can enable high power density converters. The introduction of wide band-gap devices opens new possibilities to improve the performance of the traction inverter. The thermal capability and the low switching losses of silicon carbide (SiC) MOSFETs can be beneficial in comparison to classical silicon (Si) IGBTs when used in a three-phase converter [4–7] allowing a more compact design.

High-power density electric machines can be achieved by minimizing the non-active parts, such as the end-windings, and by design parameters, in particular

- high airgap flux density (i.e. magnetic loading), eg. by using high energy magnets in combination with core material with saturation at high flux density [8]
- high mechanical speed [9]
- high current loading, or high current density, while simultaneously assuring a low thermal resistance between the winding and coolant

For the sake of high magnetic loading, the development of electric drivetrains is dominated by the permanent magnet synchronous machine (PMSM) [10], characterized by its high power density as well as high efficiency [11–13]. The use of rare earth magnets, such as NdFeB, in combination with flux concentration rotor structures, such as the V-shaped interior permanent magnet (IPM) rotor, allows to reach high peak airgap flux densities (up to 1 T) [11, 12]. Industrial core materials can operate typically up to 1.6-1.8 T, limited by high saturation and losses. There are materials, such as cobalt-iron, that enable higher flux densities, up to 2-2.2 T. However, higher cost and iron losses limits the use of these materials to aerospace and niche applications such as motor-sports [14]. As of today, with the current available materials, there is an upper limit when it comes to magnetic loading.

Rotating electrical machines generated output torque is proportional to the size, assuming the same current and magnetic loading condition [11, 12]. This

means that the output power and the mechanical rotating speed, for a fixed size machine, are linearly related. So it is convenient, from a specific power perspective, defined as power per weight ratio, to aim for high mechanical rotational speed. The upper limit is usually given by the yield strength of the rotor materials, the bearings capability, the core and copper AC losses which increase with the electrical frequency as well as the ability of the converter to operate at very high frequencies [15, 16]. Furthermore, a gearbox is required to match the required wheel rotational speed with the traction machine rotor speed. The higher the machine speed, the higher the needed gear ratio (number of gear stages) which can add complexity and cost to the drivetrain. Typically, maximum speeds for traction machines are in the range of 12000-18000 rpm [17].

To reach even higher power density, as identified in [18], the machine needs to be able to withstand high current density. A lot of research and engineering efforts are dedicated to "improved thermal materials", as well as "advanced cooling/thermal management techniques to reduce size, cost and improve reliability" as summarized well in [19–21]. An apparent aim is to try to bring the coolant medium closer to the main sources of heat, i.e. the stator core and winding, as opposed to so called cooling jackets. One interesting development comes from high thermally conductive epoxy potting materials. These are used for example in the rail industry to improve heat conduction and electrical isolation as well as to increase the mechanical stiffness (and damp vibrations) [22].

Enabling high current density, which in turn means high joule losses in the winding, at peak operation, does not prevent the traction machine from achieving high energy efficiency. The reason is that during driving, the machine operates most of the time in part-load, i.e. the low torque region, as shown for several drive cycles in [23] and in Chapter 5. Achieving high energy efficiency can significantly extend the driving range of the vehicle for a given battery pack.

Electrical machine windings can be divided in two main categories, distributed windings (DW) and non-overlapping fractional slot concentrated windings (FSCW) also referred as tooth-coil winding machines (TCWMs). With TCWMs, it may be possible to devote some of the space in the slot that is normally used for active material (conductors), for cooling channels instead, without sacrificing performance. Consequently, it may offer high torque density and high efficiency [24–26] when combined with a permanent magnet (PM) rotor, as well as low manufacturing cost. In [27], a 12-slot 8-pole interior-magnet TCWM for traction applications is compared with a distributed winding, a switched reluctance, and an induction

machine. The TCWM is shown to perform best in terms of torque density, even without considering the shorter winding overhang. Efficiency-wise, the two PM machines are comparable, TCWM being slightly better in the low speed region and less efficient at high speeds compared to the DW machine.

Permanent magnet synchronous machines are found in most electric vehicles available on the market today. An overview of the main specifications of some of the traction machines found in the automotive industry, which can be considered state-of-the-art, are presented in Table 1.1.

Table 1.1: Overview and performance for traction machines in automotive industry

	Tesla Model 3	BMW i3	Toyota Prius IV	Chevy Bolt	Audi A3 e-tron
Year	2017	2016	2017	2016	2014
Peak torque [Nm]	348	250	163	360	330
Peak power [kW]	202	127	53	150	75
Base speed [rpm]	4800	4500	3400	3500	-
Max speed [rpm]	18100	11400	17000	8810	6000
Active volume [l]	5.32	6.35	2.21	4.11	5.56
Gross volume [l]	12.7*	14	4.7*	8.7*	10.3*
Type of cooling	Jacket, shaft	Jacket	Jacket	Jacket	Jacket
Type of winding	Distributed	Distributed	Hairpin	Hairpin	Concentrated
Net power density [kW/l]	38	20	24	36.5	13.5
Gross power density [kW/l]	16*	9.1	11.3*	17.2*	7.3*
Net torque density [Nm/l]	65.5	39.4	73.8	87.6	59.4
Gross torque density [Nm/l]	27.5*	17.9	34.9*	41.4*	32.1*
Reference	[28]	[28, 29]	[28]	[28, 30]	[28]

*These values are derived based on the assumptions presented in Appendix A

The machines presented in Table 1.1 are all radial flux machines and present different types of winding, including the hairpin winding, a type of distributed winding. The power densities, both net (calculated considering active length and the outer stator diameter) and gross (volume of complete electric machine including the non active parts and the housing) are shown in Table 1.1. These have been specified using the volume and not the weight (the power to weight ratio is defined as specific power) due to the uncertainty in the weight data found in the literature. Furthermore, typically, the weight to volume ratio does not vary much for radial flux machines. The Tesla Model 3 and Chevy Bolt machines are the ones presenting the highest power densities. It is important to highlight that there is a degree of uncertainty in the comparison due to the fact that it is not stated under which conditions the peak torque and peak power values are valid. The Chevy Bolt machine peak torque can be held for about 25 s for a 70°C temperature rise [30], the coolant flow rate is unknown. No such information could

be found for the other machines in Table 1.1. By looking at the net torque density, and assuming that the magnetic loading is not so different among the machines analyzed, it can be noticed that the hairpin machines achieve the highest values thanks to the high copper space factors achieved. These machines, however, are typically limited in mechanical speed due to AC losses in conductors. The Tesla machine combines good values of torque density with a high base and maximum mechanical speed.

The aim of the machine design presented in this work, when engineered for mass production, is to reach values of gross power densities comparable to the ones shown in Table 1.1, thus comparable to the best in class found in the EV industry.

1.3 Review of previous work

Some interesting traction motor designs using TCWMs are presented in [31–35], however, without the integration of direct cooling in the stator, continuous current densities above 20 A/mm^2 are hardly reached, which limits the torque density, and in turn the power density.

Several proposals of high performing direct cooling techniques for TCWMs can be found in the literature.

- A double layer tooth coil winding machine concept with in-slot cooling between the coils is presented and partly evaluated in [36]. This solution uses the space in the slot not filled with copper to create cooling channels by using water-soluble mould cores, a concept that is hard to adopt for mass production.
- Using conductive pipes in the slots, with the drawback of generating large eddy current losses [37]
- Theoretical evaluation of the concept of flushing the entire stator and rotor with oil coolant [38]
- Direct-water cooled coils by winding a coolant carrying steel pipe with Litz wire, validated in a 205 kW machine for a bus application [39]. The prototype presented uses Litz wire with a tube for liquid inside each turn, which is complicated to manufacture and yet the maximum feasible current density 14 A/mm^2 at 2 l/min is reported.
- A direct winding heat exchanger is used in between the coils of a double

layer tooth coil would machine in [40]. Current densities of 25 A/mm^2 continuous and 40 A/mm^2 peak operation are reported with this solution, with coolant flow rates up to 5.3 l/min and 5.1 kPa pressure drop. Copper heat exchangers in the slot, however, can be challenging when it comes to slot insulation and manufacturing, and the authors have not presented a complete rotating machine in hardware with their cooling concept.

- The authors of [41, 42] present an in-slot cooling for a switched reluctance machine using a fluid guiding structure and airgap sealing to allow for oil cooling within the slots. The concept is tested with DC current up to 22 A/mm^2 and a flow rate of 6 l/min, however this concept comes with some challenges regarding coolant leakage to the rotor.

An emerging electrical machine technology, which has proven very effective in terms of power density, is the yokeless axial flux machines combined with liquid cooling. In particular YASA and Magnax have been showing solutions with gross power densities of over 25 kW/l (10 kW/kg) [17]. These numbers are impressive and are as of now the highest values found for commercial products within the traction power industry. However, an issue of the yokeless axial flux machine with surface mounted PMs is the low field weakening capability which typically forces an oversizing of the electric machine.

1.4 Purpose of the thesis and contributions

A cooling solution combining

- in-slot cooling, using the new available high thermally conductive potting materials to create the cooling channels
- direct iron cooling, by having stator yoke cooling channels
- design of the end section to properly distribute the oil flow to form a high turbulence region which leads to very high cooling capability of the end windings

is missing in the literature. Furthermore, the solutions found in the literature are often interesting concepts at a prototype level but hardly implementable with a low cost manufacturing process.

The main purpose of the work presented in this thesis is to investigate the different aspects of the multiphysics modelling of brushless PM machines and present a specific design of a traction machine with high cooling capabilities meant

for mass production. The targets of the design are to achieve high efficiency and power density compared to the state of the art. The focus is on radial flux tooth coil winding machines with integrated direct cooling. A novel solution is proposed, built and tested showing promising results in terms of torque and power density and a good agreement with the performance predicted both by analytical equations and numerical methods. The solution is presented in *Paper VII*, *Paper IX*, *Paper X* and in Chapter 3 of this work.

Other related activities are conducted and presented. A simplified numerical approach to modelling of cooling jackets for electrical machines is validated through thermal measurements and presented in *Paper V*. Also, a MOSFET inverter conduction loss prediction model is presented and validated experimentally with a SiC MOSFET inverter in *Paper VIII*. Finally, a system model of the converter, machine and the cooling circuit is built to analyze the performance of the system at different coolant flow rates and driving conditions. The model is also used to compare the cooling solution proposed in this work with an external cooling jacket in Chapter 5.

Below follows a more detailed description of the main contributions:

- A strategy to select pole and slot combinations from both a bottom-up (from performance evaluation of pole slot combinations) and top-down (from the specifications) design criteria for double layer tooth coil winding machines is proposed. (*Paper II*)
- A procedure based on analytical expressions to size brushless AC PM machines based on split ratio is proposed, quantifying how with constant current density there is a clear trade-off between torque density and efficiency, with the cost optimum usually laying in-between. (*Paper III*)
- A novel cooling design for tooth coil winding machines is presented, analyzed and validated experimentally. The novelty consists in the integration of the cooling within the stator, using a thermally conductive epoxy resin to create the channels within the slot, the positioning of the stator yoke cooling channels as well as the design of the end section to cool the end windings. (*Paper VII*, *Paper IX*)
- It is shown how the manufacturability of a machine such as the one mentioned in the previous point can be improved with the use of a linear winding machine that pre-winds the coils on a bobbin. This could potentially lead to a reduced manufacturing cost for high volume production, depending on

the automation level of the process. The various steps of the manufacturing process are analyzed and improvements to make the machine mass producible are proposed. (*Paper X*)

- The implementation of three different custom made calorimetric set-ups to validate the efficiency and losses is presented. The measurement system solution and components adopted can be valuable for other researchers in the field. (*Paper V*, *Paper VII*, *Paper VIII*, *Paper IX*)
- A simplified numerical approach to the analysis of electrical machines with cooling jackets is presented and validated experimentally. (*Paper V*)
- A quantification and derivation of the energy efficiency, with focus on conduction losses and the consequence of reverse conduction for a MOSFET inverter is presented and verified using a three-phase SiC MOSFET inverter suitable for traction applications. (*Paper I*, *Paper VIII*)
- A system level comparison of the cooling solution proposed and an external cooling jacket, using experimentally validated convection heat transfer coefficients, is performed in terms of efficiency and internal machine temperatures varying the flow rate of the coolant and with different drive-cycles. (Chapter 5)

1.5 Thesis outline

The thesis is structured as a collection of articles, which means that the main part of the work is found in the papers attached at the end of the thesis. The thesis includes a clarification concerning how they are interrelated, some additional design aspects which are not found in the papers, a drivetrain cooling system study and a summary of the results.

In Chapter 2, the scientific and industrial context of the traction electrical machine drive technology is discussed with a particular focus on cooling and tooth coil winding machines. Furthermore some relevant theory about PMSM and thermal modelling is outlined.

Chapter 3 outlines the design and sizing of a tooth coil winding PM machine with a novel cooling concept which has been built and tested. Starting from the vehicle performance requirements all the way to the manufacturing details.

Chapter 4 covers the three calorimetric set-ups which have been used for experimental validation of the analytical and numerical models for both machines

and MOSFET inverter, summarizing the main results achieved.

Chapter 5, presents a system model and analysis of the electric drivetrain with a particular focus on thermal and cooling aspects. The system model is built with lumped parameter thermal models and loss maps and is used to evaluate performance of different cooling strategies depending on the driving conditions.

Chapter 6 presents the main conclusions regarding the work presented and suggested future work.

1.6 List of publications

This thesis is based on the work contained in the following papers. A contribution statement is added when the author of this work is not the first author and main contributor of the papers listed.

Paper I - A. Acquaviva and T. Thiringer - *Energy efficiency of a SiC MOSFET propulsion inverter accounting for the MOSFET's reverse conduction and the blanking time.* Published in *European Conference on Power Electronics and Applications (EPE'17 ECCE Europe)*, Sept. 2017.

Paper II - S. Skoog and A. Acquaviva - *Pole-Slot Selection Considerations for Double Layer Three-phase Tooth-Coil Wound Electrical Machines.* Published in *International Conference on Electrical Machines (ICEM)*, Sept. 2018.

Contribution to the idea and structure of the paper as well as the manuscript writing.

Paper III - A. Acquaviva - *Analytical Electromagnetic Sizing of Inner Rotor Brushless PM Machines Based on Split Ratio Optimization.* Published in *International Conference on Electrical Machines (ICEM)*, Sept. 2018.

Paper IV - S. Lundmark, A. Acquaviva and A. Berqvist - *Coupled 3-D Thermal and Electromagnetic Modelling of a Liquid-cooled Transverse Flux Traction Motor.* Published in *International Conference on Electrical Machines (ICEM)*, Sept. 2018.

Minor contribution being involved in the review and part of the writing.

Paper V - A. Acquaviva, O. Wallmark, S. Lundmark, E. Grunditz and T. Thiringer - *Computationally Efficient Modeling of Electrical Machines with Cooling*

Jacket. Published in *IEEE Transactions on Transportation Electrification*, Vol. 5, Issue 3, p. 618-629, Sept. 2019.

Paper VI - A. Acquaviva, E. Grunditz, S. Lundmark and T. Thiringer - *Comparison of MTPA and Minimum Loss Control for Tooth Coil Winding PMSM Considering PM and Inverter Losses*. Published in *European Conference on Power Electronics and Applications (EPE'19 ECCE Europe)*, Sept. 2019.

Paper VII - A. Acquaviva, S. Skoog and T. Thiringer - *Design and Verification of In-slot Oil-Cooled Tooth Coil Winding PM Machine for Traction Application*. Published in *IEEE Transactions on Industrial Electronics*, Early Access, 2020.

Paper VIII - A. Acquaviva, A. Rodionov, A. Kersten, T. Thiringer and Y. Liu - *Analytical Conduction Loss Calculation of a MOSFET Three-Phase Inverter Accounting for the Reverse Conduction and the Blanking Time*. Published in *IEEE Transactions on Industrial Electronics*, Early Access, 2020.

Paper IX - A. Acquaviva, S. Skoog, E. Grunditz and T. Thiringer - *Electromagnetic and Calorimetric Validation of Direct Oil Cooled Tooth Coil Winding PM Machine for Traction Application*. Published in *Energies*, Vol. 13, Issue 13, 3339, 2020.

Paper X - A. Acquaviva, S. Skoog and T. Thiringer - *Manufacturing of tooth coil winding PM machines with in-slot oil cooling*. Published in *International Conference on Electrical Machines (ICEM)*, Aug. 2020.

Paper XI - A. Rodionov, A. Acquaviva and Y. Liu - *Sizing and energy efficiency analysis of a multi-phase FSCW PMSM drive for traction application*. Published in *IECON20*, Oct. 2020.

Contribution with the machine model, analysis of results and part of manuscript writing.

Electrical machines state of the art and modelling

The traction electrical machine is where the electromechanical energy conversion takes place and ideally this must happen in the most efficient way, occupying the least space (and consequently being as light as possible), it needs to last for the whole life of the vehicle and the overall cost and environmental impact should be as low as possible. Additionally, other features are required, such as low noise and vibrations, easiness in the control and in the recycling of materials. The design process aims at finding the best trade-off among several of these requirements for the specific application.

2.1 Traction electrical machines state of the art

Traction electric drives can be categorized in numerous ways, for instance by the electrical machines in use, the number of machines per vehicle and the placement of the traction machines within the vehicle. Regarding the traction machine, the ones mainly found are induction machines and PM (or brushless) synchronous machines. Currently there is no technology that is proven best. The brushless synchronous machine typically presents higher efficiency, power factor and power density compared to the induction machine. In the latter, losses generated in the rotor by the induced currents are a substantial part of the total losses, affecting directly the efficiency and often requires special rotor cooling. However, the efficiency of the induction machine can improve significantly with copper rotor bars, shown in Fig. 2.1. The main advantage of the induction machines comes from not having the permanent magnets, which otherwise when used in other

machine types introduce some challenges such as:

- Risk of demagnetization at high rotor temperatures
- Electromotive force (EMF) unregulated over-voltage in case of a fault
- Substantial iron losses (power loss in the steel laminations) during coasting and in the low torque region
- High cost of the rare earth materials
- Environmental impact of rare earths mining and processing
- Significant cost in the mounting process
- Depending on the speed special magnet retention techniques might be required

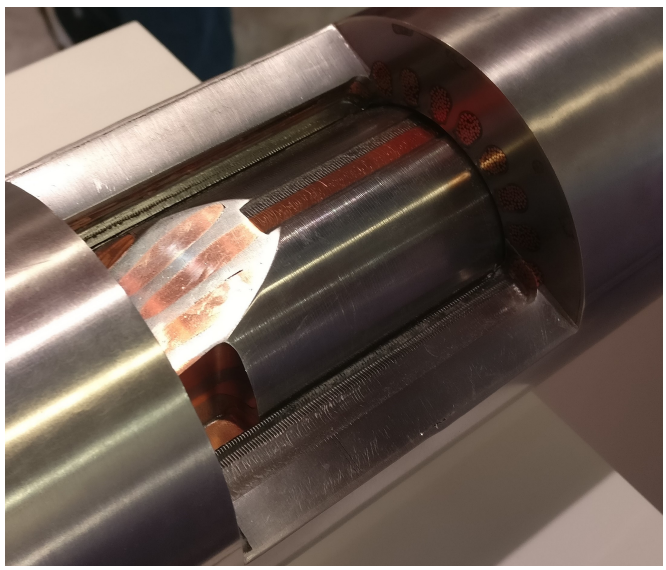

Figure 2.1: A cut open induction machine with copper rotor bars.

The most common machine type in the traction automotive industry is the brushless ac machine [10], which can be further divided by the rotor type and by the winding type. The rotor type presents many alternatives but mainly interior PM and PM assisted synchronous reluctance rotors are used. As mentioned in the introduction chapter, for the winding types there are two main alternatives, distributed winding and fractional slot concentrated windings, also defined as a tooth coil winding. Machines with these two types of windings are comparable in performance.

One type of distributed winding which is currently state of the art in many traction applications is the hairpin winding, shown in Fig. 2.2. This presents a simplified manufacturing process by insertion and good copper space factors, also known as fill factor. However, this technology is limited only to a low number of turns (pins) per stator slot and it requires welding at the end connections of the pins which complicates the manufacturing. Furthermore, there are problems of ac losses in the conductors at high rotational speeds, i.e. at high frequencies.

Figure 2.2: Hairpin winding with welded and potted end connections on one side.

2.1.1 Tooth coil winding machine

Tooth-coil wound machines, also known as non-overlapped fractional slot concentrated winding (FSCW) synchronous machines, offer several benefits compared to machines with a distributed winding, but they also present some special characteristics resulting in design concerns not typical for classical distributed winding machines. The tooth coil winding presents the following advantages:

- Short end windings
- Low noise and torque ripple [24, 25] (this depends very much on pole slot combination)
- Low manufacturing cost [26]

- High slot copper space factor achievable, especially if combined with a segmented stator (such as plug-in teeth or joint-lapped core) [24, 25]
- High values of stator leakage inductance [43, 44]. A high value of d-axis inductance enables to de-flux the machine with less current
- Reduced fault vulnerability due to lower mutual inductance between phases [43]

While the main drawbacks are:

- The winding factor which is proportional to the Torque/Ampere ratio is lower compared to the DW machine [45]
- Space harmonics generate additional losses in the rotor core and PMs, these can be significant, especially at high speeds [24, 25]
- Some pole/slot combinations can produce unbalanced magnetic forces [46]
- Sub-harmonics may cause low dominant vibration modes which may result in high acoustic noise and vibration
- It is typically hard to reach high saliency values due to high values of leakage and harmonic inductance. This usually limits the ability to have a significant amount of reluctance torque, which becomes very important in the field weakening region

When it comes to the production process, tooth coil winding machines present several options. A pole chain stator is shown in Fig. 2.3 and a segmented teeth stator is shown in Fig. 2.4. Some of these options, such as the pole star with yoke ring, single poles with yoke ring and the stator without pole shoes, present the opportunity of pre-winding the coils on bobbins and inserting them. This can reduce greatly the production time and cost by using a spindle winding machine. There are mainly three types of winding machines:

- Spindle winding or linear winding machine
- Flyer winding machine
- Needle winding machine

A cost analysis of the winding manufacturing process and assembly is very important during the design of the machine and is dependant on the number of units per year to be produced. The higher the number of units, the more it is worth investing in a fully automated process and designing a machine that can fit the process. The variables are many to be considered, to mention some: number of

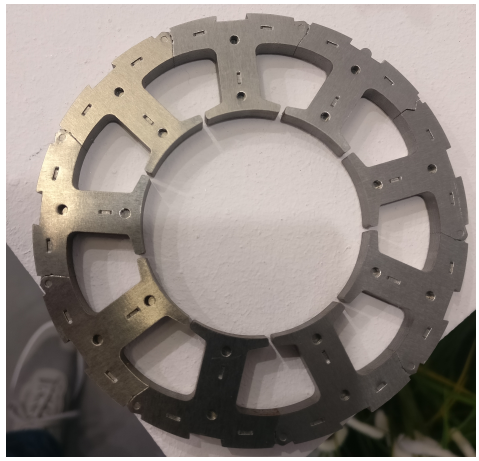

Figure 2.3: Pole chain stator.

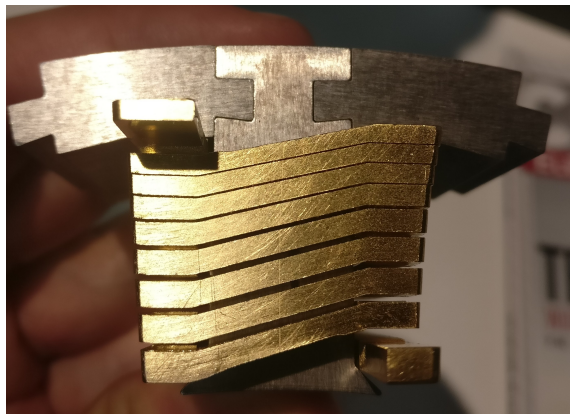

Figure 2.4: Segmented stator, the stator teeth and yoke are put together after inserting the preformed coil.

coils per motor, achievable copper space factor, number of internal coil connections, wire diameter and number of parallel strands. The needle winding machine, for example, allows to wind the stator coils of the same phase without disconnecting the wire and can easily manage to wind machines that have coils connected in parallel. With the spindle winding machine, a coil is produced by winding the wire on a rotating body at very high speeds and many coils can be produced in parallel with a single machine. An overview of motor winding technology showing different applications can be found in [47].

2.2 Permanent magnet synchronous machine electromagnetic model

Electrical machine voltage models can either be expressed using flux linkages Ψ or currents i as state variables. For synchronous machines it is convenient to express the model in the dq reference frame, synchronous with the rotor. The dynamic model of the PM synchronous machine in the dq reference frame, using flux linkages as state variables, can be written using the complex notation as [48]

$$\underline{v}_{\mathrm{dq}} = R_{\mathrm{s}}\underline{i}_{\mathrm{dq}} + \frac{\mathrm{d}\underline{\Psi}_{\mathrm{dq}}}{dt} + \mathrm{j}\omega\,\underline{\Psi}_{\mathrm{dq}} \tag{2.1}$$

$$T = \frac{3}{2}p\Big(\underline{\Psi}_{\mathrm{dq}} \times \underline{i}_{\mathrm{dq}}\Big) \tag{2.2}$$

where $\times$ is the cross (or vector) product, R_{s} is the stator resistance, ω is the electrical angular frequency and p is the pole-pair number. The model in (2.1) and (2.2) is non-linear. In fact, the flux linkages depend on the current components

$$\Psi_{\mathrm{d}} = \Psi_{\mathrm{d}}(i_{\mathrm{d}}, i_{\mathrm{q}}) \tag{2.3}$$

$$\Psi_{\mathrm{q}} = \Psi_{\mathrm{q}}(i_{\mathrm{d}}, i_{\mathrm{q}}) \tag{2.4}$$

It is often convenient to express the PM synchronous machine model using the currents as state variables. This because currents are often used in closed looped feedback control as these are much easier to measure with respect to flux linkages. The flux linkages can be expressed introducing the inductance matrix $\mathcal{L}$ and considering that by definition the PM rotor Ψ_{PM} flux is oriented on the d-axis

$$\underline{\Psi}_{\mathrm{dq}} = \Psi_{\mathrm{PM}}(i_{\mathrm{q}}) + \mathcal{L}\underline{i}_{\mathrm{dq}} \tag{2.5}$$

$$\mathcal{L} = \begin{bmatrix} L_{\mathrm{d}}(i_{\mathrm{d}}, i_{\mathrm{q}}) & L_{\mathrm{dq}}(i_{\mathrm{d}}, i_{\mathrm{q}}) \\ L_{\mathrm{qd}}(i_{\mathrm{d}}, i_{\mathrm{q}}) & L_{\mathrm{q}}(i_{\mathrm{d}}, i_{\mathrm{q}}) \end{bmatrix}. \tag{2.6}$$

Note that the PM flux linkage in (2.5) is dependent on the q-axis current due to the iron saturation. The voltage equation (2.1) becomes

$$\underline{v}_{\mathrm{dq}} = R_{\mathrm{s}}\underline{i}_{\mathrm{dq}} + \frac{d\underline{\Psi}_{\mathrm{dq}}}{\mathrm{d}\underline{i}_{\mathrm{dq}}}\frac{\mathrm{d}\underline{i}_{\mathrm{dq}}}{dt} + \mathrm{j}\omega\Big(\Psi_{\mathrm{PM}}(i_{\mathrm{q}}) + \mathcal{L}\underline{i}_{\mathrm{dq}}\Big). \tag{2.7}$$

The flux linkage components partial derivatives are called incremental inductances [48]

$$\frac{d\underline{\Psi}_{\mathrm{dq}}}{d\underline{i}_{\mathrm{dq}}} = \mathcal{L}_{\mathrm{inc}} = \begin{bmatrix} l_{\mathrm{d}}(i_{\mathrm{d}}, i_{\mathrm{q}}) & l_{\mathrm{dq}}(i_{\mathrm{d}}, i_{\mathrm{q}}) \\ l_{\mathrm{qd}}(i_{\mathrm{d}}, i_{\mathrm{q}}) & l_{\mathrm{q}}(i_{\mathrm{d}}, i_{\mathrm{q}}) \end{bmatrix}. \tag{2.8}$$

Unless the machine is linear $\mathcal{L}_{\text{inc}} \neq \mathcal{L}$. For control purpose, as well as for modelling of the torque output, it is often an acceptable approximation to consider $\mathcal{L}_{\text{inc}} = \mathcal{L}$ and simplify the inductance matrix to

$$\mathcal{L} \approx \begin{bmatrix} L_{\text{d}}(i_{\text{d}}, i_{\text{q}}) & 0 \\ 0 & L_{\text{q}}(i_{\text{d}}, i_{\text{q}}) \end{bmatrix}. \tag{2.9}$$

The two inductance components $L_{\text{d}}(i_{\text{d}}, i_{\text{q}})$ and $L_{\text{q}}(i_{\text{d}}, i_{\text{q}})$ can then be mapped using numerical methods and used in the models. The torque equation can now be expressed as

$$T = \frac{3}{2} p \Big[\Psi_{\text{PM}}(i_{\text{q}}) i_{\text{q}} + (L_{\text{d}}(i_{\text{d}}, i_{\text{q}}) - L_{\text{q}}(i_{\text{d}}, i_{\text{q}})) i_{\text{d}} i_{\text{q}} \Big] \tag{2.10}$$

The first component of the torque is generated by the interaction of the PM flux and the stator current in the q-axis. The second component of the torque, also called reluctance torque, is generated by the saliency of the machine $\xi = L_{\text{q}}/L_{\text{d}}$. In isotropic machines $L_{\text{d}} = L_{\text{q}}$ and $\xi = 1$, while for IPM machines $L_{\text{d}} < L_{\text{q}}$ meaning that by utilizing a negative d-axis current both torque components are present and contributing to the output torque.

2.3 Cooling of traction electric motors and drive-trains

Traction electric systems are designed for high power density and reliability. In order to achieve this, an effective cooling system for the electrical machine is needed, typically a closed loop forced liquid cooling. The main forced cooling solutions found in automotive and rail industry can be categorized as [19, 20]:

- Cooling jacket (oil or water)
- Hollow shaft (oil or water)
- Direct winding cooling (oil)
- Fluid bath (oil)
- Fluid spray (oil)

Some of these are compatible and applied in the same machine.

Depending on the solution in use, there are different options when it comes to the coolant fluid, as shown in [20]. Most solutions use either oil or water (either pure water or with glycol). The main characteristics of these two coolants are

- Oil has a higher boiling point than water, so it can be used to cool the machine even at a temperature of 100°C or higher. However, water-cooling may also exceed 100°C if pressurized or wixed with a certain glycol percentage content.
- Oil is an electrical insulator, thus it can be in direct contact with the winding. Also, a leak from the cooling channel to the airgap would not cause any hazard. If coolant water should similarly leak, substantial machine damage might occur.
- Oil is already present as a lubricant in the transmission and naturally helps to prevent corrosion.
- Oil has a viscosity which is higher (and with a significant temperature dependence) compared to water, meaning that more pumping power is needed to circulate the fluid.
- The specific heat of water or water/glycol is about twice that of oil, so a given flow rate of water absorbs more heat per degree increase in temperature than the same flow rate of oil.

2.4 Thermal modelling of electrical machines

Depending on the phenomena to be observed and the level of accuracy required, the modelling of electrical machines can be done at different complexity levels. The main issue in modelling a fully coupled electromagnetic and thermal problem is the different time constants. The thermal time constant can be many orders of magnitude higher than the electrical one. A common approach to multiphysics modelling of electrical machines is to solve the electromagnetic model separately from the thermal model and eventually iterate.

Electrical machine thermal analysis can be divided into two basic methods: analytical lumped-parameter (LP) circuit and numerical methods. Although the LP approach has the speed advantage, the main effort is in the determination of the parameters of the circuit model [49, 50] and usually it is limited to well known geometries. With numerical analysis, computational fluid dynamics (CFD) and finite element analysis (FEA), any machine geometry can be modeled. However, this can be demanding in terms of model setup and computational effort. Often numerical methods are used for the determination of the parameters in the analytical model [50, 51]. There are several possible approaches to thermal

modelling:

1. LP thermal model based on geometry, material data and empirical formulas for convection heat transfer coefficients
2. Thermal FEA with empirical formulas for convection heat transfer coefficients
3. LP with partial FEA and/or CFD, where some critical parts of the machines are modelled to increase accuracy. This is sometimes referred to as co-simulation
4. Computationally efficient model of liquid cooling coupled with FEA thermal modelling, presented in *Paper V*
5. Coupled 3D CFD and thermal FEA with iterations between the physics, presented in *Paper IV*

The list presented is created based on increasing computational effort and/or complexity of the machine/cooling geometry to be modelled. The phenomena of interest can differ among the models. With increasing complexity, more details can be observed. For example, the velocity distribution within the cooling channels or the distributed heat transfer coefficient on the walls of the cooling channels can only be determined by performing a CFD.

Furthermore, when implementing real-time observers or running extensive power-train optimization algorithms, the thermal model implemented needs to be reduced even to a lower level of computational effort. Two methods found in literature to do this are:

1. Eigenmodes simulation of the thermal dynamics
2. Reduced LP thermal model

The first method is based on the derivation of the eigenmodes from a full 3D thermal simulation. An example of this implementation for a traction electric machine has been presented recently in [52]. The second method is to reduce the LP network to the minimum number of nodes. An implementation of node reduction is presented in [53], showing a reduction from seven to three nodes without losing accuracy in the point of interest.

2.4.1 Lumped-parameter network - thermal parameters

In a lumped-parameter thermal model, the different parts of the electrical machine or inverter are treated as lumps assuming spatially uniform material properties

between nodes and a constant temperature in the part represented by each node [54]. The thermal capacitance of a node, modelling a region with n solids of different materials, assuming uniform heat capacity of the materials can be found as

$$C_{\mathrm{th}} = \sum_{i=1}^{n} V_{\mathrm{i}} \rho_{\mathrm{m,i}} C_{\mathrm{p,i}} \tag{2.11}$$

where ρ_{m} and C_{p} are respectively the specific mass and specific heat of the material, and V is the volume. The thermal resistance due to heat conduction along a line l for a region with varying area A perpendicular to the direction of the heat flow can be calculated as

$$R_{\mathrm{th}} = \int_0^l \frac{1}{\lambda A(x)} dx \tag{2.12}$$

where λ is the thermal conductivity. If the area is constant along the line this integral becomes

$$R_{\mathrm{th}} = \frac{l}{\lambda A}. \tag{2.13}$$

While for a segment of a hollow cylinder, the thermal resistance in the radial direction, (2.12) becomes

$$R_{\mathrm{th}} = \frac{ln\left(\frac{r_{\mathrm{out}}}{r_{\mathrm{in}}}\right)}{\lambda \theta l_{\mathrm{cyl}}} \tag{2.14}$$

where r_{out} and r_{in} are respectively the outer and inner radius of the hollow cylinder segment, θ is the segment angle and l_{cyl} is the length of the cylinder. The thermal resistance due to heat convection is calculated as

$$R_{\mathrm{th}} = \frac{1}{hA} \tag{2.15}$$

where h is the convection heat transfer coefficient. More details about heat transfer modelling can be found in [55].

2.5 The calorimetric measurement method

Calorimetry is a recognized means for the direct measurement of losses in liquid cooled power electronics and electrical machines. It can be used to overcome difficulties related to measuring a small relative difference between input and output power by a direct loss measurement. For a generic device under test (DUT) the losses can be directly estimated by measuring the mass flow rate and the temperature of the liquid at the inlet and outlet of the DUT using the simplified steady-flow thermal energy equation

$$P_{\mathrm{loss}} = C_{\mathrm{p}} \dot{V} \rho_{\mathrm{m}} \Delta\Theta \tag{2.16}$$

where C_p is the heat capacity at constant pressure of the coolant, $\dot{V}$ is the volumetric flow rate, ρ_m is the specific mass of the fluid and $\Delta\Theta$ is the temperature difference between the inlet and the outlet. Note that C_p can have a significant temperature dependence for fluids such as oils.

It is of great importance to minimize the heat leakage of the DUT to the ambient to get an acceptable accuracy in the measurements. This is usually done for power electronic converters by using closed calorimetric boxes with internal controlled temperature and for the electrical machine by thermally isolating the machine frame and flange.

Design of the tooth coil winding traction PM machine

This chapter covers the sizing and design of the traction electrical machine for a passenger car. Starting from the vehicle description, the design specifications of the traction machine are defined and used for sizing. Then both electromagnetic and thermal design are analyzed, describing the main choices and trade-offs.

3.1 Vehicle description and design specifications

In this section, the design specifications for the traction machine are derived from the vehicle performance requirements. The reference vehicle is a 2-seater small city car with the specifications and performance requirements shown in Table 3.1. A fixed gear ratio between the axis and the electrical machine is assumed. The gearbox gear ratio is calculated as $G = 8.4$ assuming a base speed of the motor of 3600 rpm at 50 km/h vehicle speed and a maximum allowable motor speed $\omega_{\max}$ of 11000 rpm at 150 km/h vehicle speed. The machine needs to be sized to fulfill the three requirements listed in Table 3.1 in terms of acceleration and gradability considering an additional mass of 200 kg (two passengers plus luggage). The three requirements are represented in Fig. 3.1, in red, together with the machine outcome of the sizing process which is also converted into force at the wheels and achievable vehicle speed, in blue. This is showing how all the required operating conditions can be covered by the proposed machine size. The green curve presents a conservative way to calculate the 0-100km/h acceleration time with three different acceleration steps, each lasting 4 s.

Table 3.1: Vehicle performance requirements

Quantity	Symbol	Value
Curb mass	m_c	800 kg
Front cross sectional area	A_{vh}	2 m^2
Top speed	v_{max}	150 km/h
Aerodynamic drag coeff.	C_d	0.3
Rolling resistance coeff.	C_r	0.009
Wheel radius	r_w	0.31 m
Starting gradability	-	25 %
Hill climbing ability	-	90 km/h at 6% and 1 m/s^2
Acceleration 0-100 km/h	-	12 s

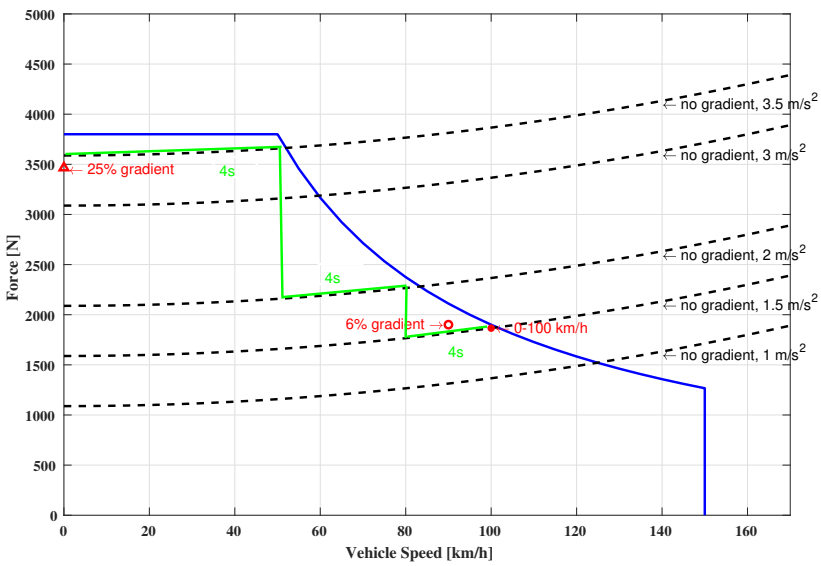

Figure 3.1: Vehicle performance requirements in red and electrical machine sizing in blue. The green curve represents the 12 s acceleration to reach 100 km/h.

Standard laminated steel materials, such as M235-35, result in reasonable core losses with an excitation frequency of 0.1-1.0 kHz. Furthermore, to have a low current ripple, the switching frequency is assumed to be at least 20 times the fundamental. For IGBT converters, the switching losses of the converter should be

limited by limiting the converter switching frequency to maximum 20 kHz. The switching frequency can be higher if MOSFETs are used but it is still important to keep the fundamental within a reasonable frequency to limit core losses. For the reasons above, the maximum fundamental frequency is set to $f_{\mathrm{f,max}} = 1$ kHz. The maximum number of pole pairs can then be calculated as

$$p_{\max} = \frac{2\pi f_{\mathrm{f,max}}}{\omega_{\max}} \tag{3.1}$$

resulting in 5.4, meaning that the maximum number of pole pairs is set to 5. The EM input design specifications are listed in Table 3.2. As a conservative approach, thanks to the intended high performance cooling, the machine is sized such that it can withstand the peak conditions for 30 seconds, assuming that its starting winding temperature is 100°C. The value for maximum temperature of the coolant in Table 3.2 is assumed based on typical values found in industry. The maximum winding temperature is set assuming a class H insulation and the dc bus voltage of 600 V is based on typically used electric vehicles battery voltages between (250 V and 800 V).

Table 3.2: Electrical machine design specifications

Quantity	Symbol	Value	Unit
Peak torque 30 s	$T_{\max}$	140	Nm
Peak power 30 s	$P_{\max}$	60	kW
Base speed	ω_{b}	3600	rpm
Max speed	$\omega_{\max}$	11000	rpm
Coolant max Temperature	$\Theta_{\mathrm{max,c}}$	60	°C
Max winding Temperature	$\Theta_{\max}$	180	°C
DC bus voltage	V_{dc}	600	V

As a reference, a similar small city car such as the new Smart Fourtwo, which has a curb mass of 880 kg and is available fully electric, mounts a 66 kW synchronous machine.

3.2 Machine design

The sizing procedure used for the main investigated motor is outlined in *Paper III*. The rotor has been chosen as an internal V-shaped PM rotor with air barriers similar to the Toyota Prius electric motor. The reasons for this choice are mainly

the saliency which improves the field weakening characteristic, the mechanical robustness of the solution and the lower PM losses, compared to a rotor surface magnet solution, thanks to the iron between the magnets and the airgap.

The coil disposition and geometries of the stator and rotor with details about disposition of conductors and cooling channels are shown in Figure 3.2. The 12 slot 10 pole machine has a key winding factor of 2 [25], meaning that each phase coil consists of two electrically series connected coils on adjacent teeth. Each coil has 28 turns, which allows for a 1.6 mm diameter enameled copper wire to be used. Having a bobbin which can be inserted, limiting the conductor diameter and avoiding parallel strands, enables the use of a linear winding machine, which could significantly reduce the manufacturing cost at high volume production. Each set of two series coils are then parallel connected to form a full phase winding.

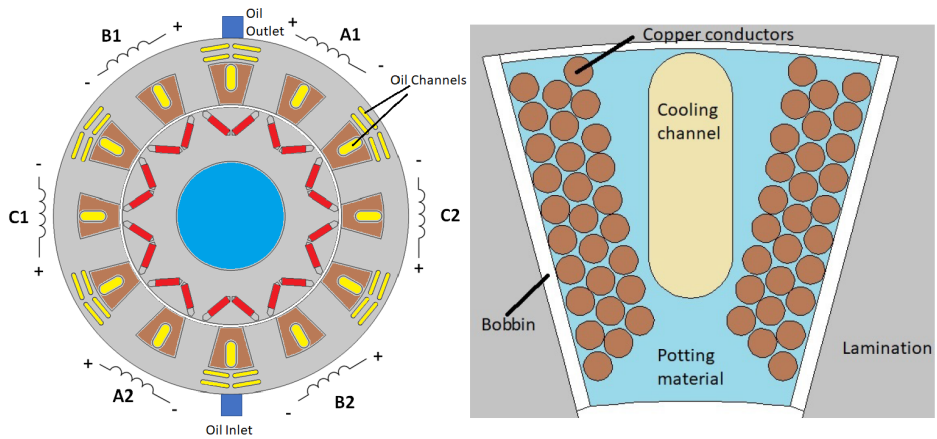

Figure 3.2: Details of lamination geometry, cooling channels and conductor disposition. Left: stator and rotor laminations geometry, coil disposition and cooling channels. Right: the arrangement of copper conductors, potting material and oil cooling channel within one slot.

The manufacturing aspects and details of the machine prototype are presented in *Paper X* together with some of the design improvements that could enable a mass manufactured product.

3.2.1 Electromagnetic Design

The electromagnetic design of the machine is covered in *Paper IX* and the choice of the pole slot combination is based on the study performed in *Paper II*. Additional

aspects not found in *Paper IX* are discussed here, in particular, field weakening properties, stator winding AC losses and demagnetization. Efficiency and loss results presented in *Paper IX* are consequently adjusted, accounting for AC losses in conductors which are shown to play a substantial role at high speeds.

Yoke Cooling channel size and electromagnetic effects

This section is extracted from *Paper VII* and *Paper IX*. Cooling channels in the stator back yoke can be introduced by removing iron after the split ratio optimisation. However, if the slot and pole combination isn't chosen properly, the yoke cooling channels might affect the electromagnetic performance negatively by increasing the reluctance path for the rotor PM flux and/or the linked flux between stator coils. The Q12p10 machine is a good choice since it features low mutual inductance between phases by linking the vast majority of the flux generated by phase windings in a loop contained within the two adjacent teeth belonging to the same phase group. This scenario is illustrated in the top part of Fig. 3.3, without the remanence PM flux and with 100 A in phase A. The change in self-linked flux due to magnetic saturation, caused by the cooling channels positioned between the phases, is negligible when channels are sized at h_{bar}=2.0 mm. Fig. 3.3 shows that the flux density in the yoke with barriers is still well below saturation values.

To find out the performance implications of flux barrier between the phases, including the PM flux, a parametric sweep FEA has been performed. The cooling channels height h_{bar} is swept from from 0.1 to 6.0 mm, corresponding to cooling channels occupying in total 2-92% of the stator back yoke height. The final design is using a 2.0 mm barrier height, as shown in Fig. 3.3. Average torque, torque ripple and iron losses are evaluated at 5000 rpm, from zero up to rated peak current; 140 A RMS (35 A/mm^2). The results for the highest current, which has the most dramatic impact, are shown in Table 3.3. The average torque output is monotonically decreasing with increasing barrier height. However, more than half of the yoke height (4.0 mm) can be cut out before 1% average torque loss is experienced. The relative torque ripple (pk2pk/avg) is kept robustly at 8% for all barrier sizes except the largest value. Moreover, the PM flux percentage reduction due to the introduction of barriers is negligible, also presented in Fig. 3.3. Regarding iron losses, when seen relative to the mechanical output power ($P_{\mathrm{iron}}/P_{\mathrm{mech}}$), a small monotonically increasing trend can be seen of less than 0.1 unit of percent from the smallest barrier to the largest. Using dual 2 mm coolant barriers positioned between the phase groups is considered to have negligible impact on electromagnetic performance, and still offer enough cross-section area

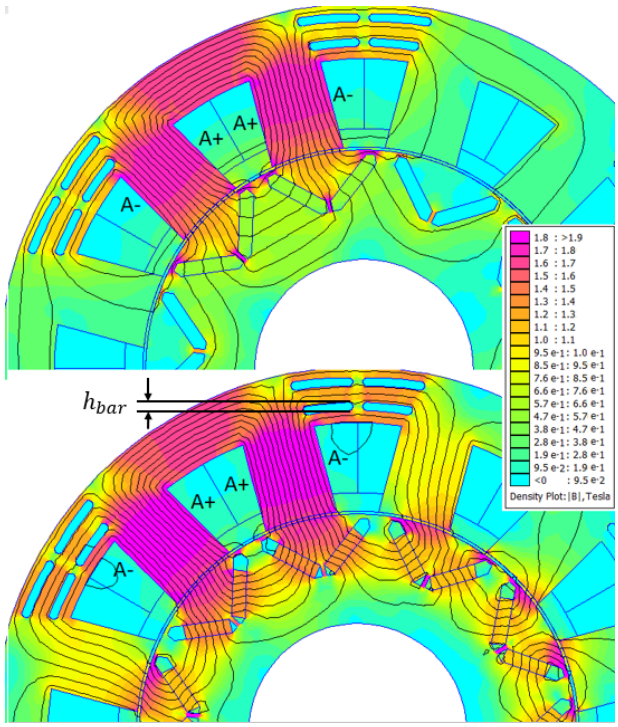

Figure 3.3: FEA established magnetic flux generated by 100 A in phase A with (bottom) and without (top) remanence flux in the magnets. h_{bar}=2 mm

for low-viscosity oil to flow without significant pressure drop. The shape of the channels and the choice of having four parallel channels instead of one is driven by flow split evaluation as presented in *Paper VII*. The resulting pressure drop is measured to 37.6 kPa at the maximum oil flow of 6.0 l/min at room temperature.

This type of utilization of part of the stator yoke to introduce cooling channels can be generalized for all TCWMs featuring a key winding factor equal to an even integer; which corresponds to an even number of adjacent tooth-coils belonging to the same phase winding as described in *Paper II*.

Table 3.3: Results from FEA evaluation of cooling barrier size at 5000 rpm, 140 A RMS (35 A/mm^2), 120° current angle. h_{bar}=0.1 mm is selected as reference for relative changes. h_{bar}=2.0 mm is chosen for the prototype machine.

Barrier height		Average torque		Torque ripple		Iron losses		PM Flux
h_{bar}	$2h_{\mathrm{bar}}/h_{\mathrm{yoke}}$			pk2pk	pk2pk/Avg		$P_{\mathrm{iron}}/P_{\mathrm{mech}}$	change
(mm)	(%)	(Nm)	(± %)	(Nm)	(%)	(W)	(%)	(± %)
0.1	1.5	145.66	0.00	12.34	8.47	980.2	1.29	0.00
1.0	15	145.62	-0.03	12.51	8.59	986.5	1.29	0.00
2.0	31	145.59	-0.05	12.24	8.41	999.0	1.31	0.00
3.0	46	145.35	-0.21	12.25	8.43	1009.5	1.33	-0.02
4.0	62	144.00	-1.14	12.03	8.35	1021.3	1.35	-0.17
5.0	77	140.04	-3.86	11.43	8.16	1006.8	1.37	-0.58
6.0	92	132.34	-9.14	14.24	10.76	958.9	1.38	-1.13

AC losses in conductors

There are several phenomena that cause additional losses in electrical machine windings [56]. These are:

- skin effect caused by current in the conductor itself
- proximity effect
- skin effect caused by an external-field
- winding element circulating currents in multi-strand conductor bunches
- phase winding circulating currents between parallel winding elements of the same phase

For the machine analyzed in this work, skin effect due to the current in each conductor itself can be neglected because the skin dept at the maximum operating fundamental frequency, calculated (combining Ampere's Law, Faraday's Law and Ohm's Law) as

$$\delta = \sqrt{\frac{\rho}{\pi f_{\mathrm{f,max}} \mu_{\mathrm{r}} \mu_0}}, \tag{3.2}$$

where ρ and μ_r are respectively the resistivity and relative permeability of copper, μ_0 is the vacuum permeability and $f_{\mathrm{f,max}}$ is the maximum fundamental frequency. The value obtained for the machine presented in this chapter is 2 mm, which is more than twice the radius of the conductor (0.8 mm). The conductors in the prototyped machine are not multi-stranded, so circulating currents among the strands do not occur. Phase winding circulating currents between parallel windings of the same phase could occur into the machine because of the parallel connection described in *Paper IX*. The cause of these circulating currents is usually some

magnetic unbalance in one of the parallel elements that induces an EMF different from the other branch. Causes of this magnetic unbalance could for example be: eccentricities, demagnetization, manufacturing differences of coils and magnets [56]. These sources of magnetic unbalance can not be predicted during the design phase so this effect is also neglected.

The two main sources of additional AC losses in the windings considered for the machine presented in this work are proximity effect and skin effect caused by an external-field. This external field in a PM machine is typically caused either by the leakage flux in the slot generated by the winding itself or by the rotor magnets through the slot opening. The latter can be even more relevant for a machine without tooth tips as the one designed in this work.

A 2D FEM model of the machine is made to evaluate the AC losses, modelling each conductor in one of the slots and accounting for eddy effects. The model is built with a dense enough mesh to capture the field change in different parts of each conductor. Fig. 3.4 shows the current density due to eddy currents distribution caused by different sources with and without stator current excitation. The no load losses generated in the windings are significant at high speeds.

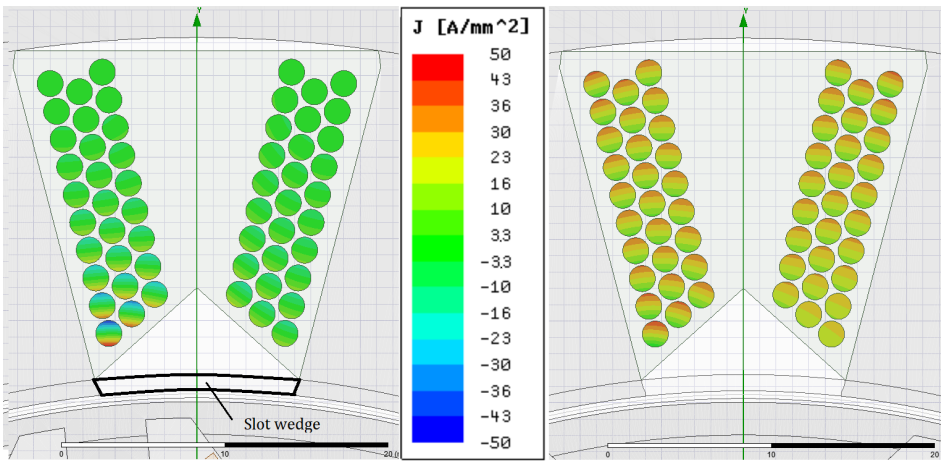

Figure 3.4: Left: current density distribution of eddy currents caused by the rotor PMs flux through the slot opening at 5000 rpm. Right: current density distribution of eddy currents caused by proximity effect and slot leakage flux at 5000 rpm and 105 A RMS.

In order to try and reduce the effect of the PM flux through the slot, the introduction of magnetic slot wedges with a relative permeability of 5 is evaluated

with FEA. The results for no-load losses and AC to DC resistance ratio, at different currents, are presented in Fig. 3.5. The magnetic wedge plays a role in reducing the no-load losses but does not affect considerably the increase in AC resistance when current is flowing. Approximately a 30 percent reduction in no-load losses and a 3 to 4 percent reduction in losses during load is possible. This is due to that the main source of resistance increase comes from the proximity effect and not from the PM field through the slot opening. Note that no magnetic wedges have been installed on the prototype. The AC winding losses are found to be significant

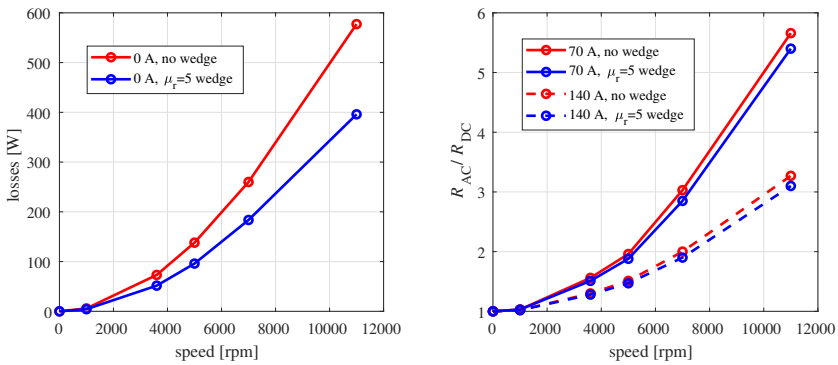

Figure 3.5: Left: AC losses in the winding at no load for the prototype design (no wedge) and with the addition of a magnetic wedge. Right: increase in resistance due to AC losses, mainly proximity effect.

and need to be modelled and included in the loss and efficiency maps. In order to do so these have been modelled analytically. The relation between AC resistance increase and speed has been found to be quadratic while inversely proportional with current. The interpolation with speed and current of the AC resistance is shown in Fig. 3.6. The fitted equation is

$$\frac{R_{\mathrm{AC}}}{R_{\mathrm{DC}}} = 1 + k_{\mathrm{fit,I}} \left(\frac{I_0}{I} \right) n_{\mathrm{rpm}}^2 \tag{3.3}$$

where the fitting coefficient for $I_0 = 70$ A is $k_{\mathrm{fit},70} = 3.8610^{-8}$ 1/rpm^2. This fitting function has been utilized in the FEA loss map results to obtain updated values. Also the AC winding losses at no load have been fitted and adjusted to be included in the loss and efficiency maps. Note that in *Paper IX*, the no load losses have been measured, however the effect of AC winding losses has been neglected and these have been included in the iron losses. A scaling factor of 2 was applied to match the iron losses found in the FEA maps. When considering

the AC winding losses this scaling factor is reduced to 1.8 so also the iron losses are slightly re-scaled here. The updated loss maps and efficiency map including the effect of AC winding losses are presented in Fig. 3.7 and Fig. 3.8. Results show how copper losses are now speed dependent and the efficiency falls below 90% in the region above 9000 rpm.

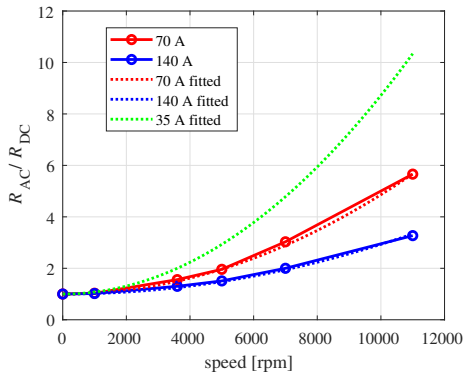

Figure 3.6: Fitting of AC resistance to speed and current.

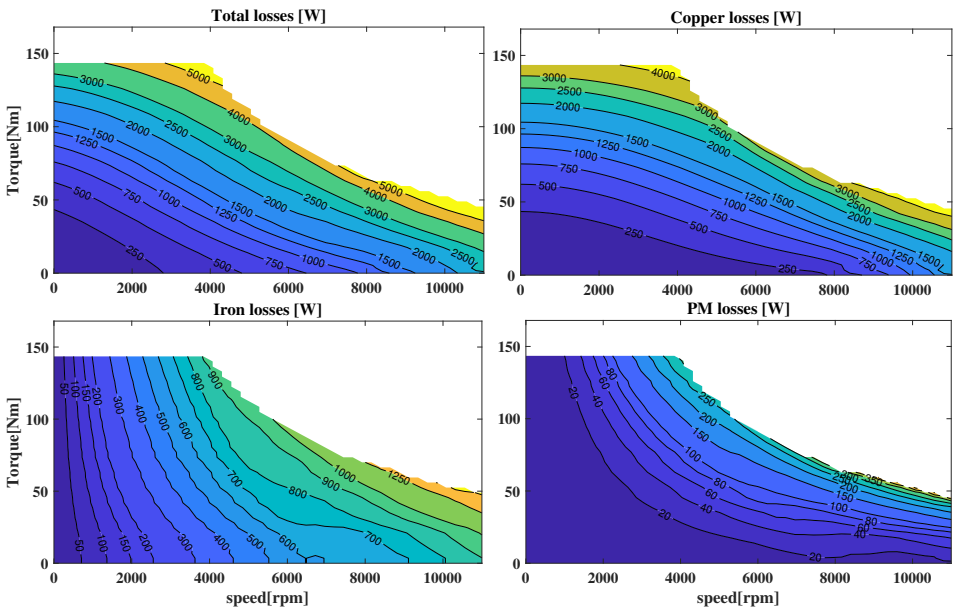

Figure 3.7: Updated loss maps including AC winding losses (relative to *Paper IX*).

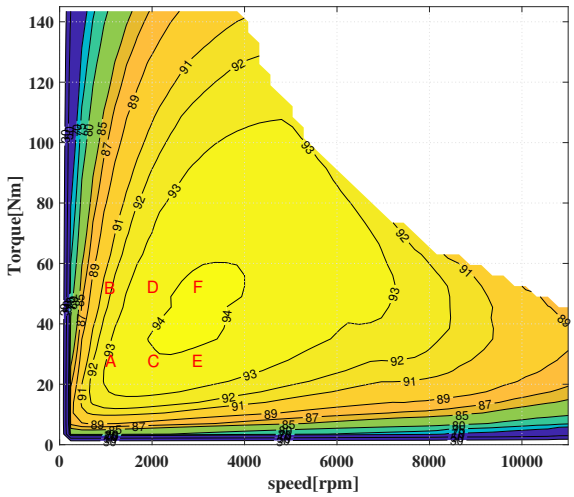

Figure 3.8: Updated efficiency maps including AC winding losses (relative to *Paper IX*). The letters in red represent the six points where the efficiency has been validated, results are reported in Chapter 4.

Field weakening and characteristic current

One important aspect for traction machines is the field weakening characteristic, in particular the maximum output power-curve in the speed region above base speed. These aspects are directly related to the machine parameters. The relevant parameters are the d and q axis inductances, the PM flux linkage, the rated voltage and maximum current. The inductances and the PM flux linkage, seen in Fig. 3.9, are not constant with the currents, and this should be accounted for when analyzing the field weakening properties, as shown in *Paper IX*. The characteristic current of the machine [57], defined as the negative d-axis current needed to completely oppose the PM flux linkage, can be calculated as

$$I_{\mathrm{ch}} = \frac{\Psi_{\mathrm{PM}}}{L_{\mathrm{d}}}. \tag{3.4}$$

Assuming that the machine is operating close to the maximum current of 140 A RMS, with the optimal maximum torque per ampere (MTPA) current angle, the parameters of the machine can be fixed to constant values, $L_d = 0.9$ mH, $L_{\mathrm{q}} = 1.35$ mH and $\Psi_{\mathrm{PM}} = 0.095$ Wb. The resulting characteristic current is $I_{\mathrm{ch}} = 105$ A, lower than the maximum current, which, according to [57], means that the machine can be completely de-fluxed and in turn reach high speeds without exceeding the

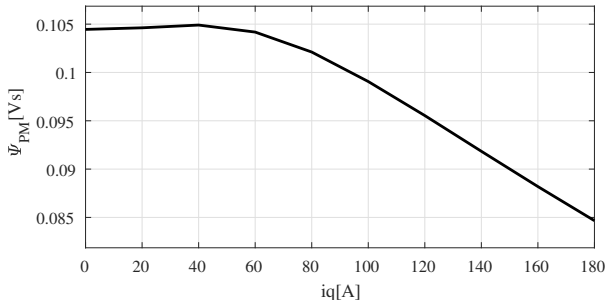

Figure 3.9: FEA results for PM flux linkage as a function of q-axis current.

rated voltage. These values can be used to analyze the machine inverter utilization on the IPM optimal design plane as a function of saliency and normalized PM flux and the maximum output power as a function of speed [57] shown in Fig. 3.10. The optimal machine design area, from a constant power speed curve perspective, lays in-between the 0.6 and 0.8 inverter utilization lines in the right plot of Fig. 3.10. The values of inverter utilization are closely related to the power factor. For low values of inverter utilization the power factor of the machine is poor, while for values close to 1 it is very hard to deflux the machine at high speed. The built machine lies close to the optimal machine design area and overall the machine constant power speed range fulfills the required specifications. Note that in *Paper VII* and *Paper IX* the machine peak power was reported to be 50 kW by considering the peak torque at base speed (3600 rpm), however this has been modified in this thesis to report the overall peak power of 60 kW which can be achieved at a speed which is slightly above 5000 rpm.

In *Paper VI* a machine with the same geometry as the prototype has been evaluated over the field weakening region with different control strategies. The two control strategies evaluated are minimum loss control (MLC) and MTPA. Note that the machine in *Paper VI* has a different voltage rating (400 V), which also meant a lower number of turns, magnets with a lower remanence flux and a higher current rating thanks to an increased diameter of each coil conductor (or several strands in parallel with a total equivalent conductor area which is increased compared to the built machine). Still most of the conclusions are applicable to the prototype built. The results presented in *Paper VI* do not account for AC losses in the windings which can reduce substantially the advantage of implementing the minimum loss control strategy. However, assuming that the AC losses are minimized during the design process by having multiple strands in parallel for each

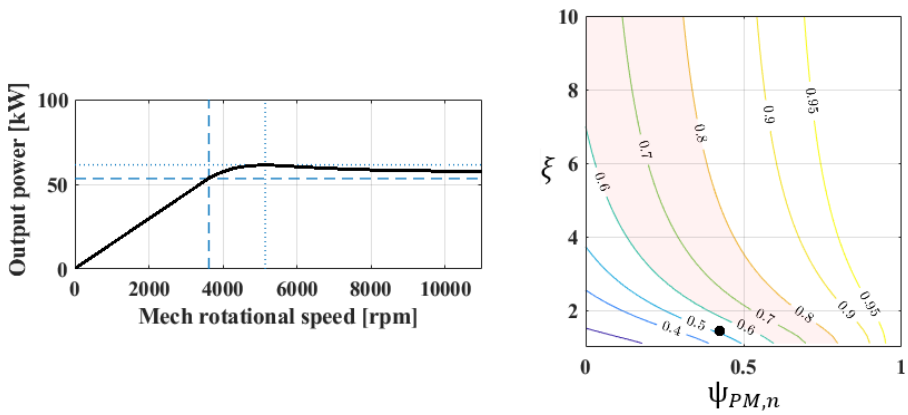

Figure 3.10: Left: maximum output power as a function of speed. Right: inverter utilization on the IPM optimal design plane as a function of saliency and normalized PM flux (black dot shows the machine in this work). [57].

conductor, the results, which show a relevant improvement in efficiency (above 10%) using MLC, are still valid.

Demagnetization

The machine should be able to withstand a converter fault without being damaged permanently. A severe condition in which the magnets could be permanently demagnetized is when the maximum current (140 A RMS) is set on the negative d-axis. In order to investigate, at the maximum current, whether the PMs are at risk of being demagnetized, a flux density plot set with the maximum amplitude to 0.55 T is shown in Fig. 3.11. The results indicate that the PM flux density does not fall below 0.55 T (magnets are of the magenta color in Fig. 3.11). According to the N48H Neodymium-Iron-Boron Magnets *BH* and *JH* curves from the manufacturer's cut sheet [58], the magnets would not get demagnetized for this fault condition, up to a temperature of 120°C, because the knee of the curve is at around 0.45 T.

The three-phase short-circuit fault at different operating points should also be investigated when studying the demagnetization. However, this is a transient condition and this verification is not performed at this stage.

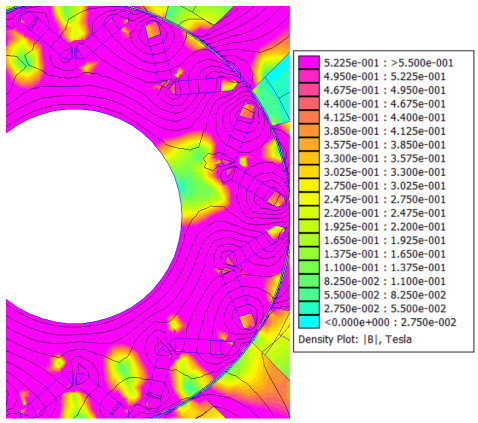

Figure 3.11: PMs flux density with maximum negative d-axis current. The plot of maximum flux density is set to 0.55 T to show where it falls below that.

3.2.2 Thermal design and cooling

The thermal design and cooling concept of the machine are covered in detail in *Paper VII*.

The stator end sections are filled with oil and flow stoppers are inserted as shown in Fig. 3.12 to redirect the oil in the two parallel paths, as illustrated in Fig. 3.13. The oil flow splits evenly thanks to the symmetry of the geometry on the two sides of the machine. The inlet and outlet are placed in correspondence to the iron cooling channels, forming parallel fluid paths with the corresponding slot channel. This is done mainly to minimize the pressure drop from the whole flow passing through those channels.

The surface temperature distribution, at 2 l/min and assuming only copper losses with a current of 60 A DC, is presented in Fig. 3.14. For the same loading condition the temperature distribution in the middle of the axial length of the machine for different flow rates is presented in Fig. 3.15.

The convection heat transfer coefficient of the channels and end winding surfaces are extracted from a 3D conjugate heat transfer simulation (using Comsol) and used in a 3D transient thermal model that can be used to predict temperatures over dynamic conditions.

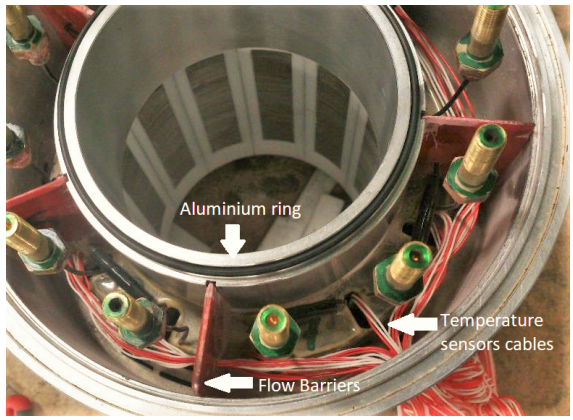

Figure 3.12: Details of manufactured machine end section at non-drive-end showing the flow barriers between the slots and the phase connection terminals.

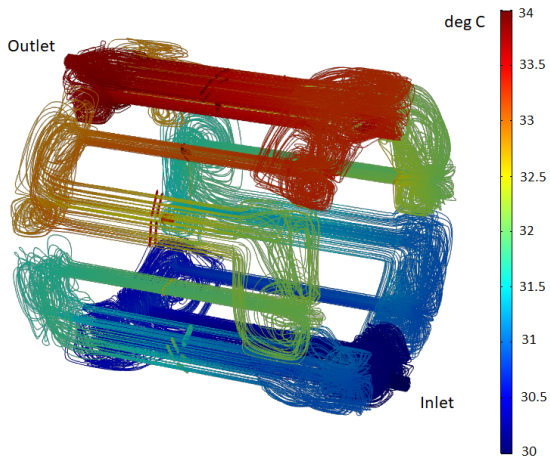

Figure 3.13: 3D conjugate heat transfer simulations. Velocity streamlines showing the coolant flow path and the temperature increase from inlet to outlet at 6 l/min, inlet oil temperature of 30°C and winding loading of 60 A DC (15 A/mm^2).

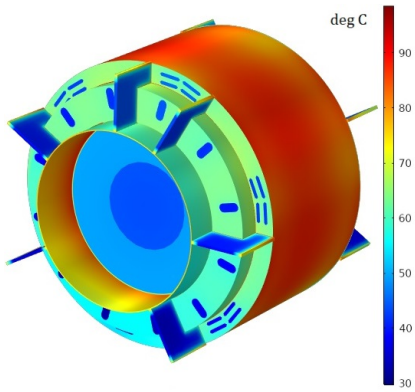

Figure 3.14: Surface temperature distribution with 60 A DC (15 A/mm^2), oil inlet temperature of 20 °C and 2 l/min flow rate from 3D conjugate heat transfer simulations.

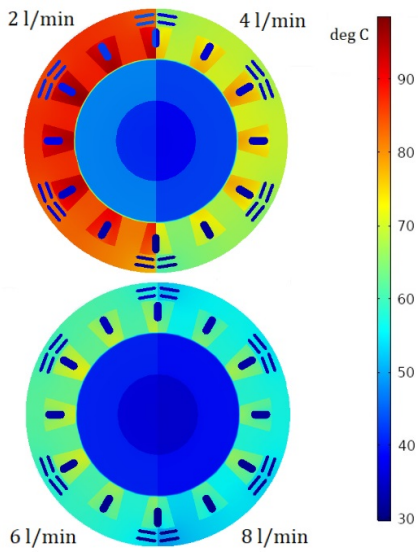

Figure 3.15: Motor temperature distribution with 60 A DC (15 A/mm^2), oil inlet temperature of 20°C and four different oil flow rates from 3D conjugate heat transfer simulations. The simulated temperatures are symmetrical for the two motor halves and hence only one half is shown per oil flow rate.

3.3 Design improvements for production version

This section is extracted from *Paper X*. The margins taken because of the hand-winding process and the sub-optimal bobbins used during prototyping led to a copper conductor of 1.6 mm in diameter. However, with a winding machine and an optimized bobbin design for series production a copper conductor of 1.8 mm is feasible, which would result in a net copper space factor of 0.57 and an increased power output of about 10% as shown in Appendix A.

Regarding the terminations and end sections these have been built with substantial margins. The flow stoppers can be integrated in the end-cap, avoiding single insertion. There is significant room to reduce the space in the end section, thus reducing the total volume and thus further improve the power density.

The external frame is used just for mechanical support and can be made thinner than the one built for the prototypes. This would allow to further reduce the mass and gross power density. A summary of the suggested design improvements for mass production is presented in Table 3.4.

Table 3.4: Design Improvements

	Prototype	Production version
Star connection	External	Internal
Parallel coil connection	External	Internal
Adjacent coil connection	Soldered	No interruption
Coil former	Single	Multi-former tool
Bobbins	Water cut	Molded
Winding	Manual	Linear winding machine
Temperature sensors	Yes	No
Wire diameter	1.6 mm	1.8 mm
End-section barriers	Single parts	Integrated in end-cap

Test set-ups and measurements

In this chapter, three different custom calorimetric set-ups are outlined. The set-ups have been built and utilized in the measurements to validate the models and the designs presented. Furthermore, the main results from the measurements are reported.

- Set-up 1 is the one built to test and validate the machine prototype described in Chapter 3 and used for experimental validation in *Paper VII* and *Paper IX*.
- Set-up 2 was built to validate a thermal model, developed during a research visit at KTH, on a machine with an external cooling jacket described in *Paper V*
- Set-up 3 was built to validate the analytical conduction model for the three phase inverter developed in *Paper VIII*

4.1 Set-up 1 - Main investigated machine with closed loop oil-to-water circuit

The first set-up is composed of a closed loop oil-cooling circuit with an oil-to-water heat exchanger. The machine prototype is tested in a lab environment consisting of a DC machine used as a load, power electronics, and a custom made oil-to-water cooling system. The setup is illustrated in Fig. 4.1 and a photo is shown in Fig. 4.2. Appropriate sensors are installed and calibrated to measure:

- torque T
- rotational speed n

- rotational position θ
- oil and water flow $\dot{V}$
- oil temperatures Θ
- oil pressure p
- voltages v
- currents i

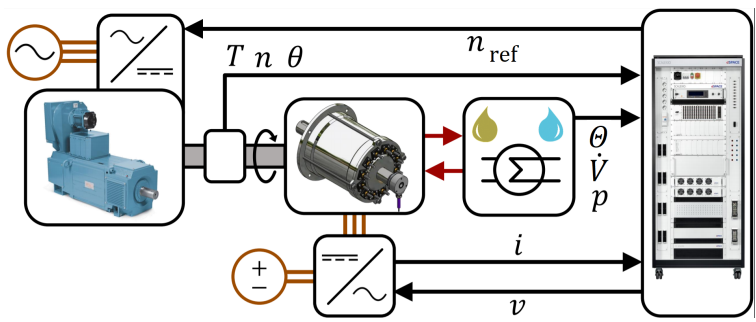

Figure 4.1: Measurement system setup with DC machine to the left, prototype machine in the middle connected to a calorimetric oil-to-water cooling system and controlled by a dSpace rack, to the right.

Tap water is flow-controlled with a feedback PI-controller into a heat exchanger to cool the oil circulated in the machine. The low-viscous oil is circulated by a 100 W controlled gear pump capable of generating 3 bar overpressure (corresponding to approximately 7 l/min flow rate). An oil reservoir and a 10 μm particle filter are also part of the oil cooling circuit. Redundant Swissflow SF-800 sensors are used for flow measurements, several NTC sensors as well as 4-wire PT-100 class A sensors are redundantly measuring oil temperatures to offer high accuracy and high reliability for the prototype setup. The entire test system is controlled and monitored through a dSpace SCALEXIO-system. The prototype machine is supplied with a three-leg IGBT-based inverter up to 600 V DC, operating at 5 kHz Space Vector Modulation closed-loop current control. The DC machine is operating at closed-loop speed control while the machine under test is operated in closed-loop current control.

The coolant oil used for the prototype machine is provided by ExxonMobil and specifically developed for electrical machine cooling, featuring low viscosity and good thermal properties as shown in Table 4.1. Note that the oil used is not

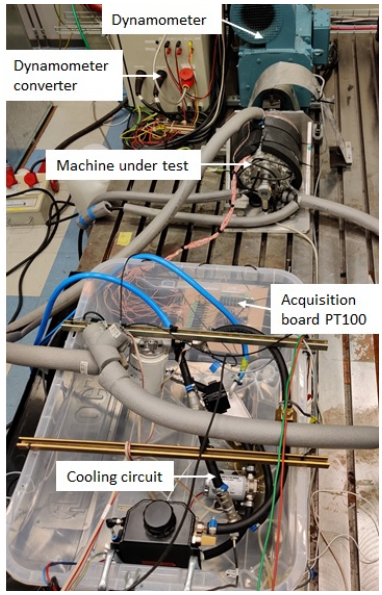

Figure 4.2: Photo of calorimetric setup and load DC machine (dynamometer).

a commercial product yet, so more details about the properties and composition are not available at the time.

Table 4.1: Oil coolant properties (data from ExxonMobil).

	40 °C	80 °C	100 °C
Kinematic viscosity (cSt)	2.31	1.28	1.02
Specific heat (J/kgK)	2.15	2.28	2.35

An example of the outcome of a calorimetric measurement is presented in Fig. 4.3. It is of great importance to reach thermal steady state in order to achieve an accurate calorimetric reading, the inlet and outlet fluid temperature should be stable as well as the flow rate to get an accurate power reading.

First, the parameters of the machine have been measured and validated: inductance, back EMF and DC resistance. A summary of the main parameters is reported in Table 4.2.

Then, the machine has been tested together with the current control loop to verify the torque output as a function of current, presented in Fig. 4.4.

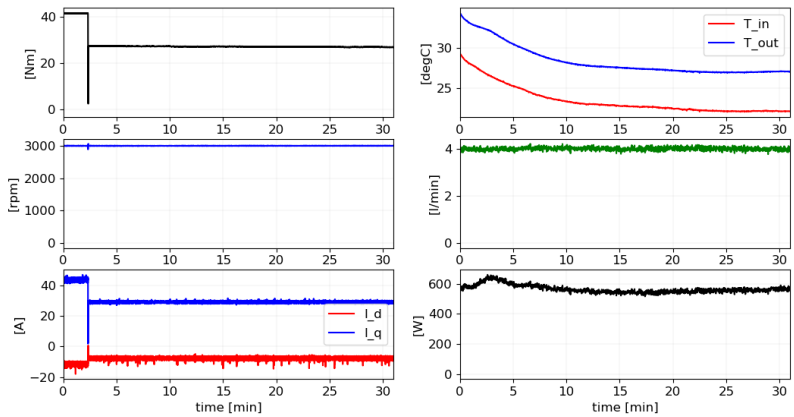

Figure 4.3: Calorimetric run at 3000 rpm and 30 A RMS. The plots are showing: top left output torque, top right oil inlet and outlet temperature, middle left mechanical speed, middle right oil flow rate, bottom left d-axis and q-axis currents, bottom right calorimetric loss, in all cases versus time.

Table 4.2: Rated and measured machine parameters.

Parameter	Value	Unit
Phase resistance	60	mΩ
Back EMF constant (line to line, peak)	0.893	Vs/rad
Base current (peak)	198	A
Base voltage (line, peak)	346	V
Base speed	3600	rpm
Base inductance	0.93	mH
d-axis inductance (non saturated)	1.2 / 1.29	mH / p.u.
q-axis inductance (non saturated)	1.7 / 1.83	mH / p.u.

The 30 second peak operation has also been validated, Fig. 4.5, as well as the efficiency for 6 different operating points using the calorimetric method in Fig. 4.6. Note that FEA results in Fig. 4.6 are updated with the AC winding losses discussed in Chapter 3. The measurements for peak torque, 140 A RMS, are carried out at an input oil temperature of 20°C and oil flow of 6 l/min. Considering that the temperature raise measured is about 60°C, the machine could withstand

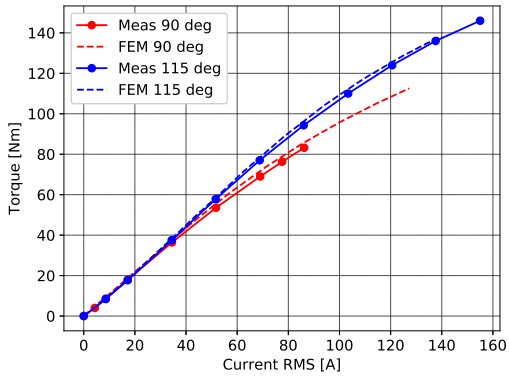

Figure 4.4: Average torque output at 150 rpm rotor speed, 90 and 115 deg current angle. Measurement and simulation comparison.

a 30 s peak operation starting with a winding temperature of 100°C.

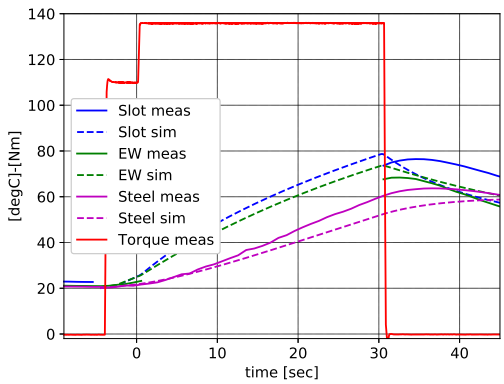

Figure 4.5: Peak torque operation (140 A RMS, 150 rpm) for 30 s at starting temperature and oil temperature of about 20°C. Solid lines showing measured values of the warmest sensor for the winding in the slot, in the end winding (EW) and on the steel. Dashed lines are simulated values.

Additionally, temperatures in the machine have been measured and compared with the 3D thermal model, with convection heat transfer coefficients of surfaces where oil is flowing, namely the cooling channels and end section. Results are presented and discussed in *Paper VII*.

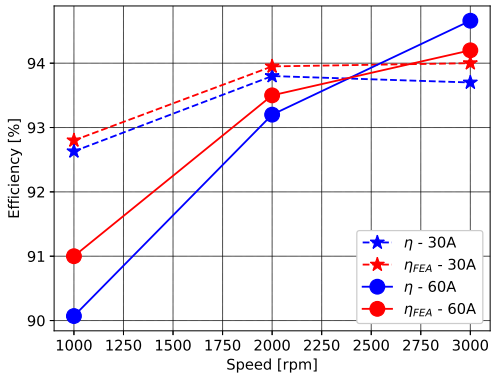

Figure 4.6: Updated efficiency comparison with measurements including AC winding losses.

4.2 Set-up 2 - Electrical machine open loop water circuit

The second set-up is an open loop water cooling circuit used to test a TCW machine with an external cooling jacket used for experimental validation in *Paper V*. For this water cooled machine, DC current calorimetric measurements at standstill have been performed. The computationally efficient thermal model is using several assumptions to simplify the model of a TCW machine thermal model and its cooling jacket.

The measurements are performed connecting all the machine coils and phases in series and supplying a dc current. The series connection of the phases ensures that the same current flows in all the coils and a uniform heat distribution is achieved. The copper losses are uniform in the winding and can be easily determined. The rotor is kept at standstill. Tap water is forced into the water jacket through hoses and controlled manually. Temperature sensors, 4 wire PT100 (Pentronic Model 7410000), are placed at the inlet and outlet of the machine such that turbulence is created in proximity to the probe for better accuracy. The machine is shown in Fig. 4.7 and the lab set up is presented in Fig. 4.8.

The main objective of this setup was mainly to validate the thermal model of the machine with the cooling jacket in transient conditions. The simulated and measured temperatures of sensors placed in different parts of the stator winding

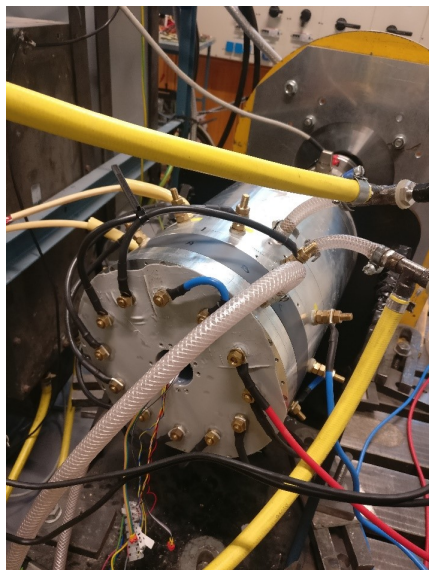

Figure 4.7: Machine prototype.

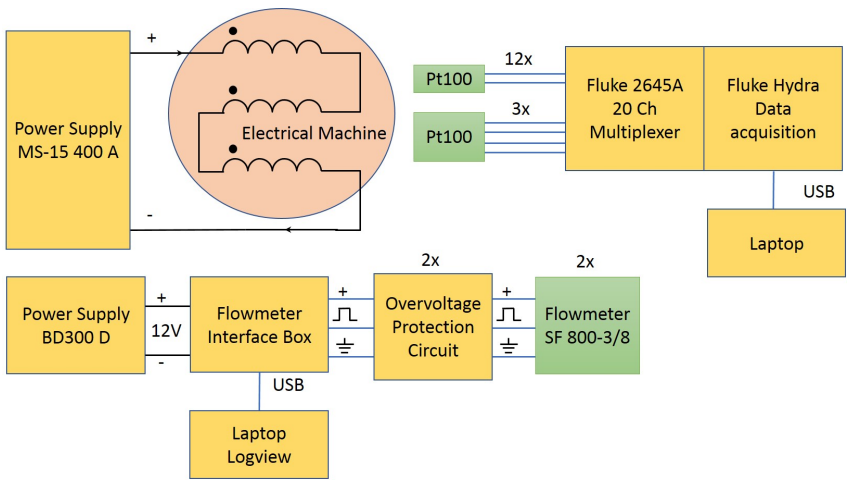

Figure 4.8: Lab set up.

are presented in Fig. 4.9 and Fig. 4.10. The slot numbering and placement can be found in *Paper V*. The temperature of the winding has been estimated with an average absolute error of 3% of the temperature rise. Considering that the model allows transient simulations, thanks to the low computational effort, it is well suited to analyze the machine behaviour with high precision in dynamic conditions.

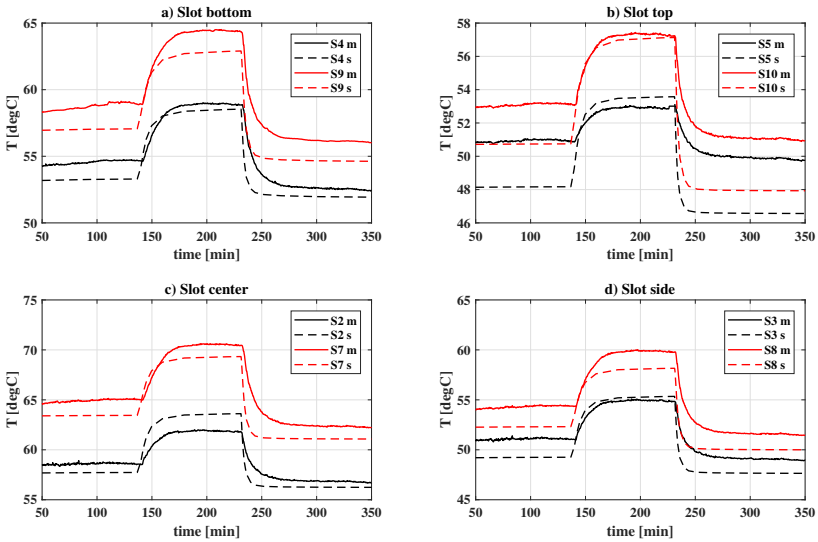

Figure 4.9: Temperature sensors in the slots. Measurements shown in solid lines (m) and simulations in dotted (s).

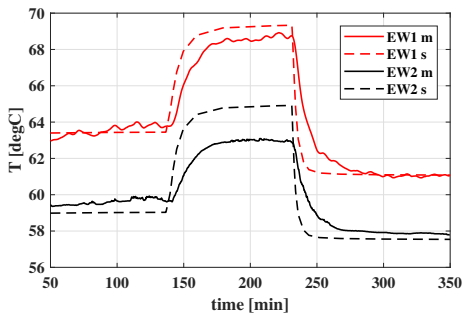

Figure 4.10: Temperature sensors in the end winding. Measurements shown in solid lines (m) and simulations in dotted (s).

A more detailed discussion of the results can be found in *Paper V*.

4.3 Set-up 3 - Power converter open loop water circuit

The third set-up is also open loop and built to directly measure the losses of power converters used for experimental validation in *Paper VIII*. The objective of the experimental set-up was to validate the analytical model of MOSFET conduction losses accounting for reverse conduction and blanking time covered in *Paper 1* and *Paper VIII*.

The double jacketed calorimetric box has an inner and an outer air chamber. Having two chambers reduces the leakage heat through the box walls. The inverter and heatsink were fitted inside the calorimetric box with high resolution temperature sensors (4-wire PT100) at the water inlet and outlet. The pump used in the setup is a medical grade pump able to operate with a high accuracy at very low flow rates. A low flow rate of 200 ml/min was chosen in order to increase the outlet to inlet water temperature difference and have a good reading accuracy of the temperature sensors. This is necessary when measuring losses in the range of 10-30 W. The complete laboratory setup is shown in Fig. 4.11.

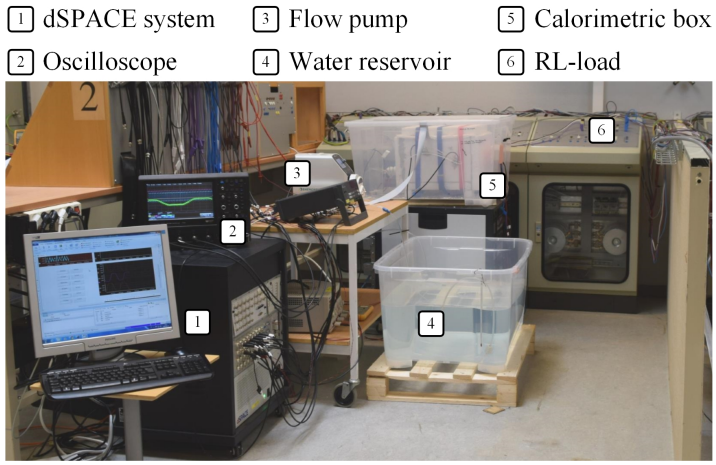

Figure 4.11: Actual test setup environment with calorimetric box, water reservoir, data acquisition and control unit.

The temperature difference between the outlet and the inlet of the calorimetric box can be seen in Fig. 4.12. In time intervals of about 1 h, the inverter was alternately operated with and without reverse conduction. It can be noted that the effect of the reverse conduction has a significant impact on the inverter

losses.

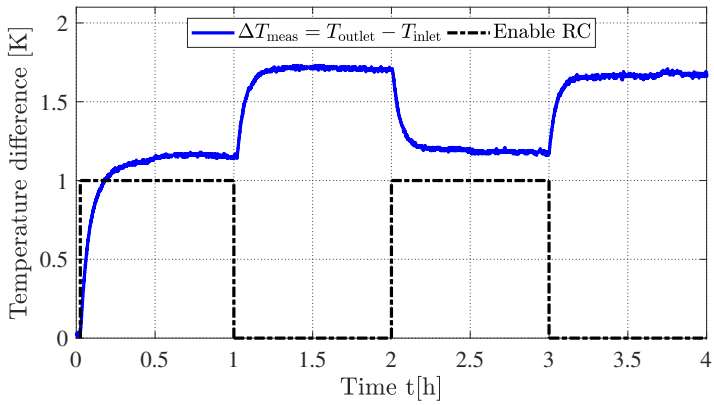

Figure 4.12: Measured water temperature difference between the outlet and the inlet with alternately enabled and disabled reverse conduction for a current amplitude of 20 A at 50 Hz.

The loss comparison between both cases, with and without reverse conduction, at thermal steady state are presented in Fig. 4.13. These show a good match between the calorimetric measurements and the analytical model as well as the relevance of accounting for reverse conduction when operating a three phase inverter.

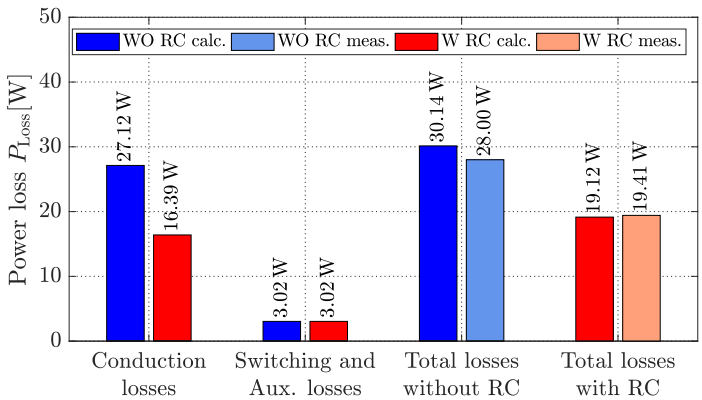

Figure 4.13: Comparison of estimated losses, using the analytical models, and measured losses for a current amplitude of 20 A at 50 Hz. W RC: with reverse conduction. WO RC: without reverse conduction.

Electric drivetrain thermal modelling and analysis

In this chapter a model of as system composed of an inverter, traction machine and the cooling circuit for an electric vehicle is presented. Two different cooling solutions for the same machine are considered in the study, one with the cooling method presented in Chapter 3 and one with an external water cooling jacket instead. The objective is to show and compare how the two cooling solutions perform at different flow rates and under different driving conditions.

The inverter modelled in this chapter is a three phase IGBT inverter using three half bridge modules with silicon carbide schottky diodes (Semikron SKM200GB12T4SiC2). The three half bridge modules are mounted on a single liquid cooled aluminium heat sink (Guasch RG82031AI).

5.1 System modelling

In this section a description of the main assumption and modelling details of the system are presented. The system model includes:

- Lumped parameter (LP) thermal models of both inverter and machine. The main assumptions and derivation of the parameters are described in Appendix B and based on derivations found in [54, 59, 60]. The machine surfaces to coolant LP convection heat transfer coefficients (also included in Appendix B) are derived from CFD simulations presented in *Paper VII* for the cooling solution adopted in the prototyped machine and in *Paper V* for an external cooling jacket used in a different PM machine. Modelling

of the latter was experimentally validated regarding internal temperature measurements. Oil is used as a coolant for direct cooling while for the jacket cooling a 50/50 water/glycol mix is used instead

- Loss, current, voltage and power factor maps of the machine derived based on the FEA presented in *Paper IX* (including the AC losses presented in Chapter 3). The maps are three dimensional and they depend on torque, speed and PM temperature. Copper loss temperature dependence on the winding temperature is also included. Copper losses are divided such that 30% is assumed in the end-winding and 70% in the active part of the winding
- Bearing losses, calculated as in [61], are dependant both on the machine torque and angular mechanical speed assuming a fixed friction coefficient
- An analytical model of the inverter losses based on the switch and diode parameters found in the manufacturer data sheets. The analytical model used for IGBT conduction and switching losses are based on models found in [62] assuming a three phase pulse width modulation (PWM) with sinusoidal voltage reference and sinusoidal current. Temperature dependence of the collector-emitter resistance and the constant voltage drop is also included
- A model of a centrifugal pump energy consumption for circulating the coolant. The pump power is assumed to be cubic with the flow rate, with a maximum consumption of 43 W at a flow rate of 8 l/min for oil at 20°C and 30 W at a flow rate of 8 l/min for a water/glycol mix at 20°C due to a lower fluid viscosity
- A constant temperature of the coolant at the inlet of the inverter, modelling an ideal radiator which is able to dissipate all the losses to the ambient

The system does not include a model of the battery and of the transmission losses.

The two machines analyzed (direct cooling and cooling jacket) have exactly the same geometry and loss, current, voltage and power factor maps. It is assumed that for the machine with the cooling jacket the coils are wound around the teeth separated by slot liners instead of using PTFE bobbins. The reason is that the PTFE bobbin is a significant thermal barrier between the coil and stator core and without direct cooling this would lead to an excessive temperature increase in the winding. A schematic overview of the system model is presented in Fig. 5.1.

The LP model for the machine with direct cooling is presented in Fig. 5.2 and the one with the cooling jacket in Fig. 5.3. Note that the thermal resistances

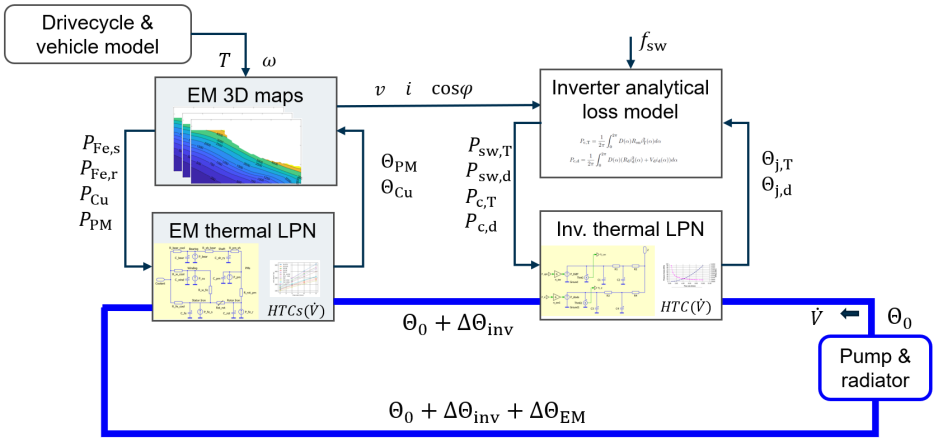

Figure 5.1: System model schematic overview

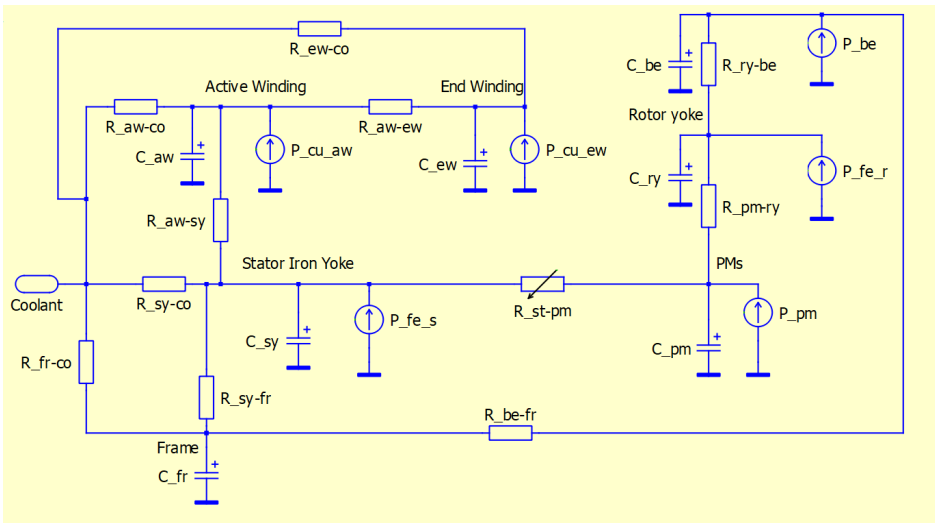

Figure 5.2: Lumped parameter network of the electrical machine with direct oil cooling (derivation of parameters found in Appendix B)

which depend on the flow rate are calculated when initializing the simulation and kept constant. Some thermal resistances are speed dependent, as described in Appendix B, and are represented with a variable impedance in the two LP models.

The inverter power module is modelled with an RC Cauer network model as presented in Fig. 5.4. The parameters are derived by interpolating the transient impedance thermal curves found in the Semikron SKM200GB12T4SiC2 data sheets.

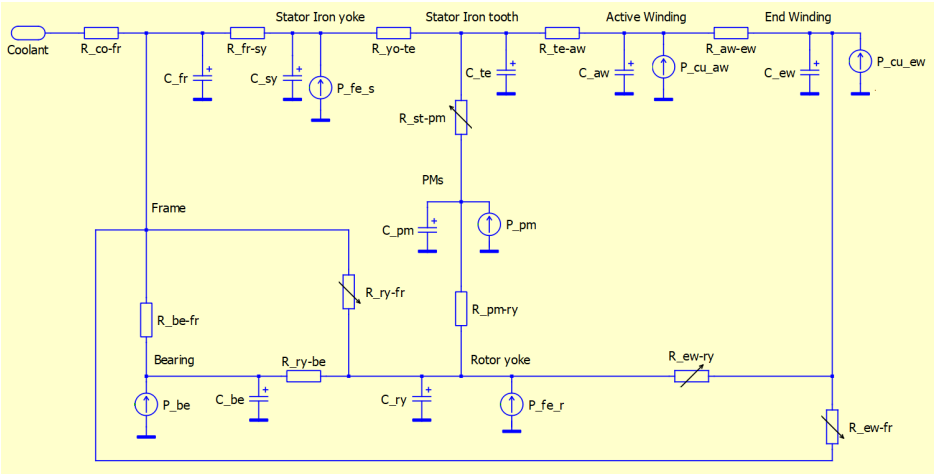

Figure 5.3: Lumped parameter network of the electrical machine with external cooling jacket (derivation of parameters found in Appendix B)

In order to use a single LP network representing the whole inverter, each thermal capacitance is multiplied by 6 (the number of switches and diodes in the inverter), each thermal resistance is divided by 6 and the total switch loss and diode loss are applied. The LP network in Fig. 5.4 is then attached to a single RC model of the heatsink with the thermal impedance and thermal resistance as presented in Appendix B.

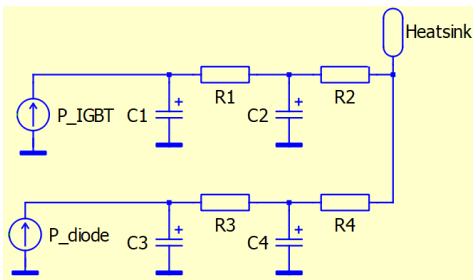

Figure 5.4: Lumped parameter RC Cauer network of the inverter power modules

5.2 System analysis

The system model described in the previous section is analyzed assuming the vehicle specifications described in Chapter 3 and three different drive-cycles. The

drive-cycles are chosen to represent different driving conditions, named urban drive, rural drive and highway drive. These are chosen from standardized drive-cycles based on the Artemis project, which involved 40 European research laboratories and was founded by the European Commission for accurate estimation of pollutant emissions from transport in different driving conditions [54]. The Artemis urban has low speed levels, 10-60 km/h, and is dense with start and stop sub-cycles. The Artemis rural cycle has speeds in the range of 50-100 km/h and sections of steady speed mixed with section of unsteady speed. The Artemis highway represent a drive with steady speed levels and some takeovers with a maximum speed of 130 km/h [54]. The three drive-cycle operating points are shown in Fig. 5.5 on the electrical machine total loss map with a PM temperature of 20°C .

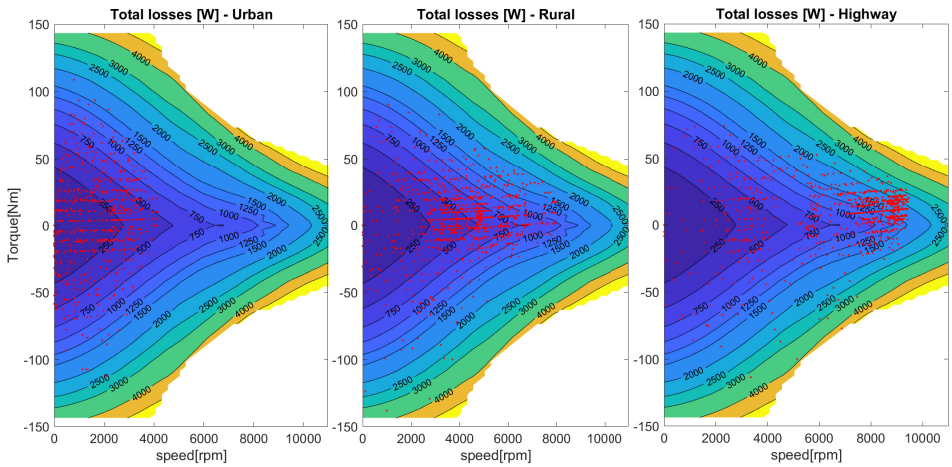

Figure 5.5: The three drive-cycle (urban, rural and highway) operating points shown on the electrical machine total loss map (with a PM temperature of 20°C)

Simulations of the system with a direct cooled machine for the three different drive-cycles are presented in Fig. 5.6 for the urban case, Fig. 5.7 for the rural case and Fig. 5.8 for the highway drive-cycle. All three are done at the external ambient temperature of 40°C, which is considered as a worst case, and assuming all the components thermal capacitances starting at ambient temperature. The flow rate is kept constant at 3 l/min for the urban and rural case and at 6 l/min for the highway drive-cycle. With these assumptions the temperatures never exceed 110°C. There is a significant temperature margin (assuming the maximum winding temperature of 180°C) even considering a potential higher initial temperature of the different components.

It is interesting to notice how the winding losses become significantly higher than the inverter losses for highway driving, in Fig. 5.8, because of the AC resistance increase at high speeds. The inverter and winding losses are proportional, the inverter ones being slightly higher, for the urban drive in Fig. 5.6 which is for the most part below base speed of the machine. Also, for rural and highway cycles the iron losses are a very relevant part in the efficiency balance of the system. Worth mentioning is that consistently with the measurements reported in *Paper VII*, the end-winding temperature is lower compared to the winding within the slot.

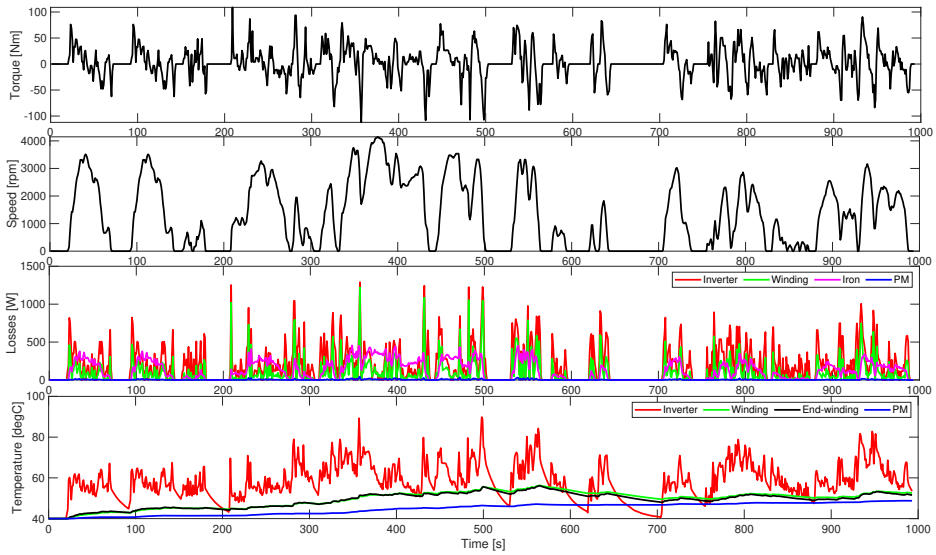

Figure 5.6: System losses and temperatures for the urban drive-cycle at 3 l/min and ambient temperature of 40°C with the direct cooled machine

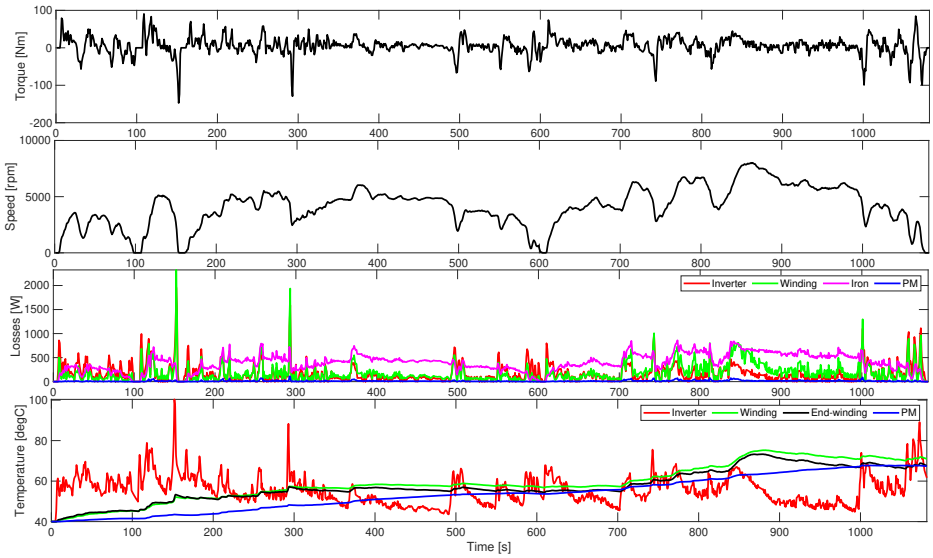

Figure 5.7: System losses and temperatures for the rural drive-cycle at 3 l/min and ambient temperature of 40°C with the direct cooled machine

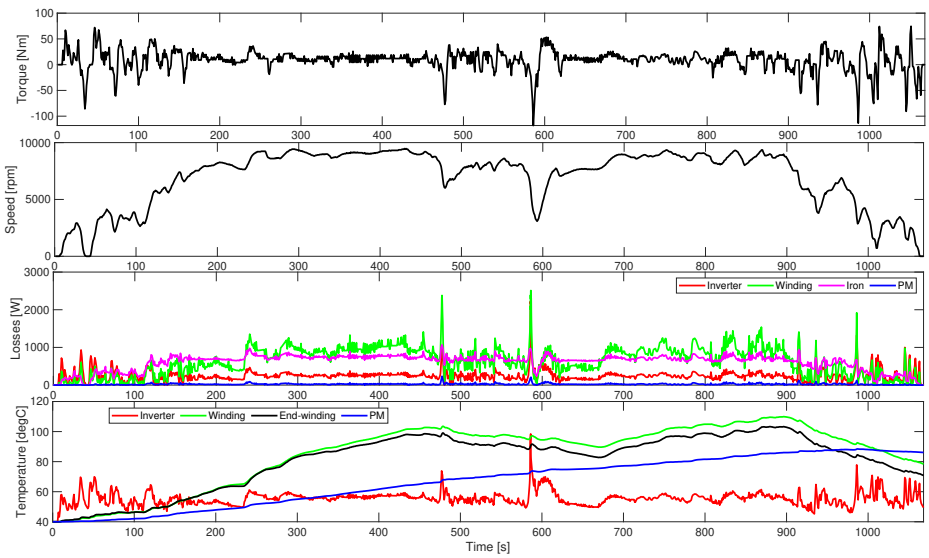

Figure 5.8: System losses and temperatures for the highway drive-cycle at 6 l/min and ambient temperature of 40°C with the direct cooled machine

5.3 Comparison - water/glycol cooling jacket vs direct oil cooling

In this section the two cooling strategies are compared based on the LP models presented in Section 5.1. The comparison is done for the three different drive-cycles at coolant flow rates ranging from 2 l/min to 8 l/min with a constant ambient temperature of 40°C. The results for the maximum and average electrical machine temperatures are presented in Fig. 5.9. The winding temperature within the slot is clearly affected by the cooling strategy along with the coolant medium used, the direct cooling being significantly more effective than the cooling jacket. Also, highway driving is far more demanding in terms of cooling compared to rural and urban driving due to the high iron and AC winding losses at high speeds. It is interesting to notice that, even by increasing the external jacket water/glycol flow to 8 l/min, the temperature of the winding is still higher than having oil flowing in the slot at 2 l/min. In the end-winding this difference is even more significant. The PM temperature is slightly higher for direct cooling in the urban and rural drive. This is mainly because the main heat path of the losses generated in the rotor is through the shaft, bearings and finally to the frame that is typically best cooled in the case of the cooling jacket. However, for the highway drive-cycle, due to the very high amount of winding and iron losses, there is a high percentage of the heat that is flowing to the rotor. This effect is more critical for the external jacket due to an increased thermal resistance between the sources of heat in the stator and the coolant compared to the direct solution. Thus, the lower temperatures of the PMs for highway driving in the case of direct cooling.

The temperature results for the inverter are presented in Fig. 5.10. Having water/glycol instead of oil and exactly the same heatsink, means that the heat exchange improves, and therefore temperatures of the inverter are lower in the case of the cooling jacket.

Two efficiency values are presented for the system. First, the average efficiency of the electrical machine during the motor operation and secondly the total energy efficiency of the system, calculated as the ratio between the useful energy to the wheels, assuming all breaking energy is regenerated, and the total energy coming from the battery. This means that the total energy efficiency of the system includes the effect of all the losses in the inverter, machine and pump as well as the effect of having several energy flows when breaking and accelerating. The results are presented in Fig. 5.11.

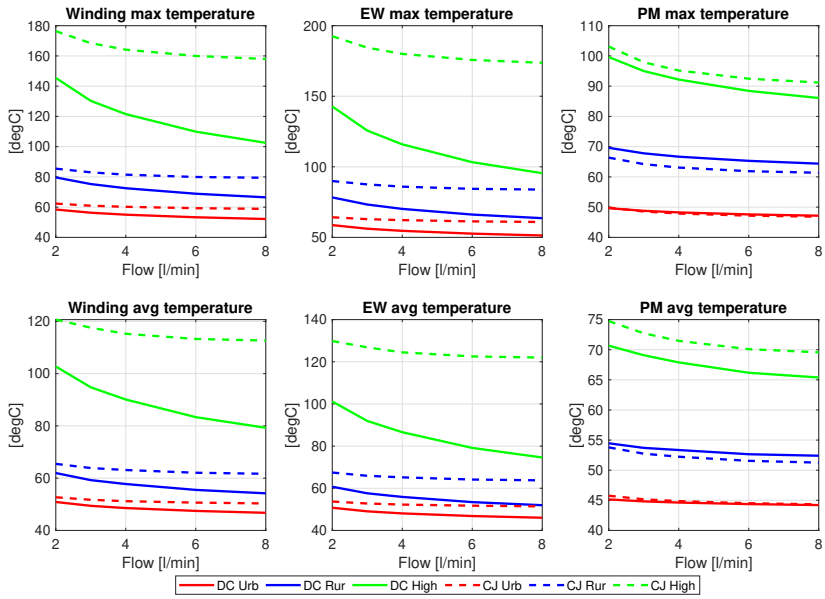

Figure 5.9: Maximum and average temperature of key nodes of the electrical machine for different coolant flow rate and drive-cycles (DC is direct oil cooling and CJ is water/glycol cooling jacket) at ambient temperature of 40°C

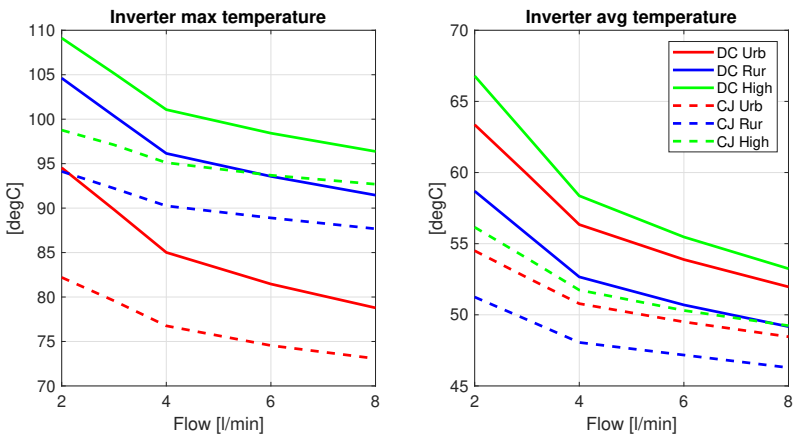

Figure 5.10: Maximum and average temperature of the inverter switch junction for different coolant flow rate and drive-cycles (DC is direct oil cooling and CJ is water/glycol cooling jacket) at ambient temperature of 40°C

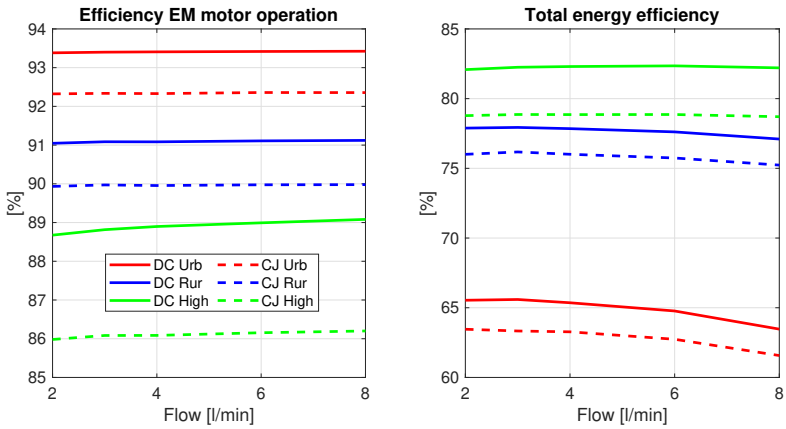

Figure 5.11: Average efficiency of the electrical machine during motor operation and total energy efficiency of the system for different coolant flow rates and drive-cycles (DC is direct oil cooling and CJ is water/glycol cooling jacket) at an ambient temperature of 40°C

With the direct oil cooling, the efficiency of the electrical machine during motor operation is about 1% higher in the case of urban and rural drive-cycles and up to almost 3% in the case of highway driving. The total energy efficiency of the system is up to 3.4% percentage higher for highway driving, 1.8% for the rural case and 2.1% for urban drive-cycles. The urban drive-cycle is the one having the lowest total energy efficiency among the three due to the large number of transfers between mechanical energy and electrical energy. Also, it is interesting to notice how the highest total energy efficiency is at low coolant flow rates, 2-3 l/min, for urban and rural driving while it is beneficial to increase the flow to 4-6 l/min for highway driving.

Similar efficiency results are presented for a constant flow rate of 4 l/min and varying ambient temperature, which corresponds to the temperature at the outlet of the ideal radiator as well as the initial temperature of the components, in Fig. 5.12. The higher the ambient temperature, the higher the advantage of having direct oil cooling in terms of efficiency, however the efficiency difference is still very relevant even at temperatures below 0°C.

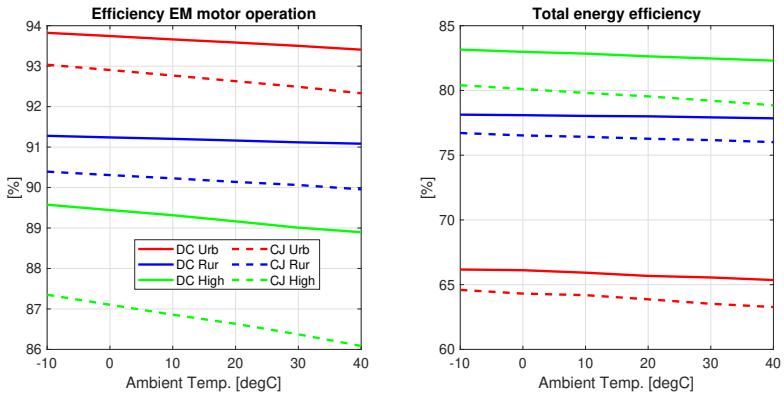

Figure 5.12: Average efficiency of the electrical machine during motor operation and total energy efficiency of the system for different ambient temperatures and drive-cycles (DC is direct oil cooling and CJ is water/glycol cooling jacket) at a flow rate of 4 l/min

Overall, considering the efficiency gain and lower internal machine temperatures, which affect the lifetime and reliability, there is a clear advantage in having a direct oil cooling solution proposed.

Conclusions and future work

This work presents the design of a tooth coil winding PMSM machine for traction application, covering the thermal and the electromagnetic design as well as performance validation. The solution adopted integrates the cooling in the stator by having oil flowing directly through the slot and the stator yoke. Original elements of this machine design are the direct-oil cooling channels positioned in the stator yoke and the direct in-slot cooling, by using a thermally conductive epoxy resin to create oil channels within the slot. The machine is designed with straight teeth, such that it is possible to use a linear winding machine to pre-wind the coils on a bobbin and insert them, potentially leading to a reduced manufacturing cost for high volume production.

It is shown that for the 12 slots 10 poles machine, the electromagnetic performance is negligibly affected when removing iron in the stator yoke for cooling channels if the position is carefully selected to the yoke area between the phase windings. Output torque, no-load voltage and inductance are measured and compared with FEA results, showing very good agreement. Furthermore, the efficiency of the machine is validated in six operating points, using a calorimetric direct-loss measurement set-up, matching with FEA within 1%. The peak efficiency is an area above 94% with a wide operating area above 90%. The model-to-measurement temperature deviations are within a few percent of the temperature increase (and within a few °C), proving the usefulness of the simplified thermal model and validating the convection heat transfer coefficients derived with the CFD anaylsis.

Two system models based on lumped parameters thermal networks and loss maps of the machine and inverter are built. One having direct oil cooling for the electrical machine and the other having an external cooling jacket with a

water/glycol mix flowing as a coolant. The results from different driving conditions and flow rates of the coolant show how the direct cooling leads to significant advantages in terms of efficiency gain. This is quantified to be between 1.5% and 3.5% points depending on the drivecycle, and internal temperatures of the machine, which could lead to an increase in the lifetime and reliability of the system.

The adopted cooling solution enables a continuous RMS copper current density of up to 25 A/mm^2 and 35 A/mm^2 for 30 seconds. Although the machine is tested at max 3000 rpm, the FEA models indicate that the target of 60 kW can be met at speeds slightly above 5000 rpm. The information presented in Table 1.1 is updated and shown in Table 6.1 with the addition of the prototype machine and a hypothetical production version engineered for mass production. The net power density of the built prototype is 24 kW/l, and gross value of 8 kW/l which can possibly be improved for series production. It is exemplified how design improvements may bring the gross power density to levels such as 15.5 kW/l.

Table 6.1: Overview and performance for traction machines in automotive industry and studied case

	Tesla Model 3	BMW i3	Toyota Prius IV	Chevy Bolt	Audi A3 e-tron	Presented prototype	Prod. version
Year	2017	2016	2017	2016	2014	2018	-
Peak torque [Nm]	348	250	163	360	330	140	154*
Peak power [kW]	202	127	53	150	75	60	66*
Base speed [rpm]	4800	4500	3400	3500	-	3600	3600
Max speed [rpm]	18100	11400	17000	8810	6000	11000	11000
Active volume [l]	5.32	6.35	2.21	4.11	5.56	2.5	2.5
Gross volume [l]	12.7*	14	4.7*	8.7*	10.3*	7.5	4.2*
Type of cooling	Jacket shaft	Jacket	Jacket	Jacket	Jacket	Direct	Direct
Type of winding	Distr.	Distr.	Hairpin	Hairpin	Conc.	Conc.	Conc.
Net power density [kW/l]	38	20	24	36.5	13.5	24	26.4*
Gross power density [kW/l]	16*	9.1	11.3*	17.2*	7.3*	8.0	15.5*
Net torque density [Nm/l]	65.5	39.4	73.8	87.6	59.4	56	61.6*
Gross torque density [Nm/l]	27.5*	17.9	34.9*	41.4*	32.1*	18.8	36.3*
Reference	[28]	[28, 29]	[28]	[28, 30]	[28]	-	-

*These values are derived based on the assumptions presented in Appendix A

When comparing the machines in Table 6.1, it is important to remember that there is a degree of uncertainty due to the fact that in most cases it is not stated in which conditions the peak torque and peak power values are calculated. The one reported for the presented machine is a 30 s peak operation which leads

to a winding temperature increase of about 60 °C at a oil flow rate of 6 l/min, whereas the Chevy Bolt machine peak torque can be held for about 25 s for a 70 °C winding temperature increase [30], the coolant flow rate is unknown. Table 6.1 shows that Tesla Model 3 and Chevy Bolt machines are the ones presenting the highest gross power densities. A production version of presented solution could reach a value of gross power density which is close to the best in class, about 3% lower than the Tesla model 3 machine and 10% lower than the Chevy Bolt.

The proposed technology has a good potential for the traction industry considering that, on top of the high values of power density, having a concentrated winding is a clear advantage in terms of production cost and reliability, as well as the low winding temperature and efficiency improvement thanks do direct cooling.

Furthermore, analytical models to quickly evaluate the conduction losses of a three-phase MOSFET inverter including the effect of the reverse conduction have been presented and experimentally validated. These models can be used as a quick and accurate tool during the inverter design process to evaluate the inverter efficiency and to perform thermal evaluations. The negligence of the reverse conduction can lead to significant errors in the conduction loss estimation, which might result in an overdimensioned cooling system. A SiC MOSFET inverter for traction applications has been tested for different operating conditions and the losses were measured using a calorimetric setup. The measured losses have been compared with the proposed analytical models showing good agreement of about 98.5%.

The following topics would be a natural continuation of the work here presented

- Test the machine prototype up to the maximum mechanical speed of 11000 rpm to verify both the field weakening capability and the efficiency at high speed
- Evaluate the effect of PWM generated time harmonics on iron and AC winding losses
- Analyze the three-phase short-circuit transient with different initial conditions
- Operate the machine prototype with a 6 phase converter and analyze the fault mode control functionality and performance as well as to try to minimize the DC capacitor current ripple (analysis of this is presented in *Paper XI*)

- Design a second version of the prototype eliminating oil leakage to the airgap, trying to improve the copper space factor by having multiple strands for each turn, which would also reduce AC winding losses, as well as trying to compact the end section

References

[1] I. E. Agency, "EU - Energy, Climate change, Environment," https://ec.europa.eu/clima/policies/transport_en, accessed on August 2020.

[2] *CAIT Climate Data Explorer via Climate Watch*. https://ec.europa.eu/clima/policies/eu-climate-action_en, accessed on August 2020.

[3] I. E. Agency, "Global EV Outlook 2017 [Online]," Accessed 2017-05-14. Available at https://www.iea.org/publications/freepublications/publication/GlobalEVOutlook2017.pdf.

[4] T. Zhao, J. Wang, A. Q. Huang, and A. Agarwal, "Comparisons of sic mosfet and si igbt based motor drive systems," in *2007 IEEE Industry Applications Annual Meeting*, pp. 331–335, Sep. 2007.

[5] H. Zhang and L. M. Tolbert, "Efficiency impact of silicon carbide power electronics for modern wind turbine full scale frequency converter," *IEEE Transactions on Industrial Electronics*, vol. 58, pp. 21–28, Jan 2011.

[6] M. Chinthavali, P. Otaduy, and B. Ozpineci, "Comparison of si and sic inverters for ipm traction drive," in *2010 IEEE Energy Conversion Congress and Exposition*, pp. 3360–3365, Sep. 2010.

[7] H. Zhang, L. M. Tolbert, and B. Ozpineci, "Impact of sic devices on hybrid electric and plug-in hybrid electric vehicles," *IEEE Transactions on Industry Applications*, vol. 47, pp. 912–921, March 2011.

[8] P. Ramesh and N. Lenin, "High power density electrical machines for electric vehicles—comprehensive review based on material technology," *IEEE Transactions on Magnetics*, vol. 55, no. 11, pp. 1–21, 2019.

[9] S. Chowdhury, E. Gurpinar, G.-J. Su, T. Raminosoa, T. A. Burress, and B. Ozpineci, "Enabling technologies for compact integrated electric drives for automotive traction applications," in *2019 IEEE Transportation Electrification Conference and Expo (ITEC)*, pp. 1–8, IEEE, 2019.

[10] E. A. Grunditz and T. Thiringer, "Performance analysis of current bevs based on a comprehensive review of specifications," *IEEE Transactions on Transportation Electrification*, vol. 2, pp. 270–289, Sept 2016.

[11] J. Pyrhonen, T. Jokinen, and V. Hrabovcova, *Design of rotating electrical machines*. John Wiley & Sons, 2009.

[12] J. R. Hendershot and T. J. E. Miller, *Design of brushless permanent-magnet machines*. Motor Design Books, 2010.

[13] K. T. Chau, C. C. Chan, and C. Liu, "Overview of permanent-magnet brushless drives for electric and hybrid electric vehicles," *IEEE Trans. on Industrial Electronics*, vol. 55, no. 6, pp. 2246–2257, 2008.

[14] M. Cossale, A. Krings, J. Soulard, A. Boglietti, and A. Cavagnino, "Practical investigations on cobalt–iron laminations for electrical machines," *IEEE Transactions on Industry Applications*, vol. 51, no. 4, pp. 2933–2939, 2015.

[15] D. Gerada, A. Mebarki, N. L. Brown, C. Gerada, A. Cavagnino, and A. Boglietti, "High-speed electrical machines: Technologies, trends, and developments," *IEEE Transactions on Industrial Electronics*, vol. 61, no. 6, pp. 2946–2959, 2014.

[16] S. Li, Y. Li, W. Choi, and B. Sarlioglu, "High-speed electric machines: Challenges and design considerations," *IEEE Transactions on Transportation Electrification*, vol. 2, no. 1, pp. 2–13, 2016.

[17] A. El-Refaie and M. Osama, "High specific power electrical machines: A system perspective," *CES Transactions on Electrical Machines and Systems*, vol. 3, no. 1, pp. 88–93, 2019.

[18] U. D. Electrical, "Electronics technical team roadmap," tech. rep., 2017.

[19] C. Alberto, L. Matteo, R. Kesavan, M. Gianpiero, and G. Massimiliano, "A review of the state of the art of electric traction motors cooling techniques," *SAE Technical Paper*, vol. 2018-01-0057, 2018.

[20] M. Popescu, D. A. Staton, B. Aldo, C. Andrea, H. Douglas, and G. James, "Modern heat extraction systems for power traction machines," *IEEE Transactions on Industry Appl.*, vol. 52, no. 3, pp. 2167–2175, 2016.

[21] Y. Gai, M. Kimiabeigi, Y. Chuan Chong, J. D. Widmer, X. Deng, M. Popescu, J. Goss, D. A. Staton, and A. Steven, "Cooling of automotive traction motors: Schemes, examples, and computation methods," *IEEE Transactions on Industrial Electronics*, vol. 66, pp. 1681–1692, March 2019.

[22] S. Nategh, A. Boglietti, D. Barber, Y. Liu, and R. Brammer, "Thermal and manufacturing aspects of traction motors potting: A deep experimental evaluation," *IEEE Transactions on Energy Conversion*, vol. 35, no. 2, pp. 1026–1035, 2020.

[23] A. Acquaviva, E. A. Grunditz, S. Lundmark, and T. Thiringer, "Comparison of mtpa and minimum loss control for tooth coil winding pmsm considering pm and inverter losses," in *2019 21st European Conference on Power Electronics and Applications (EPE '19 ECCE Europe)*, Sep. 2019.

[24] A. M. El-Refaie, "Fractional-slot concentrated-windings synchronous permanent magnet machines: Opportunities and challenges," *IEEE Trans. on industrial Electronics*, vol. 57, no. 1, pp. 107–121, 2010.

[25] S. Skoog and A. Acquaviva, "Pole-slot selection considerations for double layer three-phase tooth-coil wound electrical machines," in *ICEM '18, Alexandroupoli*, 2018.

[26] F. Libert and J. Soulard, "Investigation on pole-slot combinations for permanent-magnet machines with concentrated windings," in *Int. Conference on Electrical Machines (ICEM)*, pp. 5–8, 2004.

[27] Z. Yang, F. Shang, I. P. Brown, and M. Krishnamurthy, "Comparative study of interior permanent magnet, induction, and switched reluctance motor drives for ev and hev applications," *IEEE Transactions on Transportation Electrification*, vol. 1, pp. 245–254, Oct 2015.

[28] A. Krings and C. Monissen, "Review of trends in electric traction motors for battery electric and hybrid vehicles," *ICEM 2020*.

[29] Y. Gai, M. Kimiabeigi, Y. Chuan Chong, J. D. Widmer, X. Deng, M. Popescu, J. Goss, D. A. Staton, and A. Steven, "Cooling of automotive traction motors: Schemes, examples, and computation methods," *IEEE Transactions on Industrial Electronics*, vol. 66, no. 3, pp. 1681–1692, 2019.

[30] F. Momen, k. Rahman, and Y. Son, "Electrical propulsion system design of chevrolet bolt battery electric vehicle," *IEEE Transactions on Industry Applications*, vol. 55, no. 2, pp. 376–384, 2019.

[31] P. B. Reddy, A. M. El-Refaie, K.-K. Huh, J. K. Tangudu, and T. M. Jahns, "Comparison of interior and surface pm machines equipped with fractional-slot concentrated windings for hybrid traction applications," *IEEE Transactions on Energy Conversion*, vol. 27, no. 3, pp. 593–602, 2012.

[32] P. Lindh, J. Montonen, P. Immonen, J. A. Tapia, and J. Pyrhönen, "Design of a traction motor with tooth-coil windings and embedded magnets," *IEEE Transactions on Industrial Electronics*, vol. 61, no. 8, pp. 4306–4314, 2013.

[33] C. Dubar, *Design and analysis of a fault-tolerant fractional slot PMSM for a vehicle application*. PhD thesis, Chalmers University of Technology, 2016.

[34] J. Wang, X. Yuan, and K. Atallah, "Design optimization of a surface-mounted permanent-magnet motor with concentrated windings for electric vehicle applications," *IEEE Transactions on Vehicular Technology*, vol. 62, no. 3, pp. 1053–1064, 2012.

[35] H. Zhang, *On electric machinery for integrated motor drives in automotive applications*. PhD thesis, KTH Royal Institute of Technology, 2017.

[36] M. Schiefer and M. Doppelbauer, "Indirect slot cooling for high-power-density machines with concentrated winding," in *IEMDC '15*, pp. 2167–2175, 2015.

[37] M. N. F. Ibrahim and P. Sergeant, "Prediction of eddy current losses in cooling tubes of direct cooled windings in electric machines," *Mathematics*, vol. 7, no. 11, p. 1096, 2019.

[38] P. Ponomarev, M. Polikarpova, and J. Pyrhönen, "Thermal modeling of directly-oil-cooled permanent magnet synchronous machine," in *2012 XXth International Conference on Electrical Machines*, pp. 1882–1887, IEEE, 2012.

[39] P. Lindh, I. Petrov, J. Pyrhönen, E. Scherman, M. Niemelä, and P. Immonen, "Direct liquid cooling method verified with a permanent-magnet traction motor in a bus," *IEEE Transactions on Industry Applications*, vol. 55, no. 4, pp. 4183–4191, 2019.

[40] S. A. Semidey and J. R. Mayor, "Experimentation of an electric machine technology demonstrator incorporating direct winding heat exchangers," *IEEE Transactions on Industrial Electronics*, vol. 61, pp. 5771–5778, Oct 2014.

[41] Z. Liu, T. Winter, and M. Schier, "Direct coil cooling of a high performance switched reluctance machine (srm) for ev/hev applications," *SAE International Journal of Alternative Powertrains*, vol. 4, no. 1, pp. 162–169, 2015.

[42] Z. Liu, T. Winter, and M. Schier, "Comparison of thermal performance between direct coil cooling and water jacket cooling for electric traction motor based on lumped parameter thermal network and experimentation," in *Proceedings of the EVS28 International Electric Vechicle Symposium and Exhibition, Goyang, Korea*, pp. 3–6, 2015.

[43] A. M. El-Refaie, Z. Zhu, T. M. Jahns, and D. Howe, "Winding inductances of fractional slot surface-mounted permanent magnet brushless machines," in *Conf. Rec. IEEE IAS Annu. Meeting., Canada*, 2008.

[44] F. Magnussen, "On design and analysis of permanent magnet synchronous machines for field weakening operation," in *Doctoral Dissertation*, 2004.

[45] F. Magnussen and C. Sadarangani, "Winding factors and joule losses of permanent magnet machines with concentrated windings," *IEMDC'03*, vol. 1, 2003.

[46] Z. Q. Zhu, L. M. Jamil, and L. J. Wu, "Influence of slot and pole number combinations on unbalanced magnetic force in permanent magnet machines," in *IEEE Energy Conversion Congress and Exposition*, 2011.

[47] Marsilli, "Winding technologies," `https://marsilli.com/motor-solutions/`, accessed on August 2020.

[48] G. Pellegrino, T. M. Jahns, N. Bianchi, W. L. Soong, and F. Cupertino, *The rediscovery of the synchronous reluctance and ferrite PM motors*. Springer, 2016.

[49] P. Mellor, D. Roberts, and D. Turner, "Lumped parameter thermal model for electrical machines of tefc design," *Proc. Inst. Electr. Eng*, vol. 138, no. 5, pp. 205–219, 1991.

[50] A. Boglietti, A. Cavagnino, and D. Staton, "Determination of critical parameters in electrical machine thermal models," *IEEE Trans. on Ind. Applicat.*, vol. 44, no. 4, pp. 1150–1159, 2008.

[51] S. Nategh, H. Zhang, O. Wallmark, A. Boglietti, T. Nassen, and M. Bazant, "Transient thermal modeling and analysis of railway traction motors," *IEEE Trans. on Ind. Electronics*, vol. 66, pp. 79–89, Jan. 2019.

[52] K. Zhou, J. Pries, and H. Hofmann, "Computationally efficient 3-d finite-element-based dynamic thermal models of electric machines," *IEEE Trans. on Transp. Electrif.*, vol. 1, pp. 138–149, Aug 2015.

[53] C. Sciascera, P. Giangrande, L. Papini, C. Gerada, and M. Galea, "Analytical thermal model for fast stator winding temeperature prediction," *IEEE Trans. on Ind. Electr.*, vol. 64, pp. 6116–6126, Aug 2017.

[54] E. Grunditz, *Design and assessment of battery electric vehicle powertrain, with respect to performance, energy consumption and electric motor thermal capability*. PhD thesis, Chalmers University of Technology, 2016.

[55] F. Incropera, D. Dewitt, T. L. Bergman, and A. S. Lavine, *Fundamentals of Heat and Mass Transfer*. John Wiley and Sons, 2007.

[56] N. B. P. Ponomarev, I. Petrov and J. Pyrhönen, "Additional losses in stator slot windings of permanent magnet synchronous machines," 10.13140/RG.2.1.2081.9368.

[57] W. L. Soong and T. J. E. Miller, "Field-weakening performance of brushless synchronous ac motor drives," *IEE Proc.-Electr. Power Appl.*, vol. 141, no. 6, pp. 331–340, 1994.

[58] A. Magnetics, "Permanent magnets data-sheets," `https://www.arnoldmagnetics.com/`, accessed on August 2020.

[59] G. Kylander, *Thermal modelling of small cage induction motors*. PhD thesis, Chalmers University of Technology, 1995.

[60] J. Linström, *Development of an experimental PM motor drive*. PhD thesis, Chalmers University of Technology, 1999.

[61] *Rolling bearings catalogue. SKF*. 2018. `https://www.skf.com/binaries/pub12/Images/0901d196802809de-Rolling-bearings---17000_1-EN_tcm_12-121486.pdf`.

[62] A. Wintrich, U. Nicolai, W. Tursky, and T. Reimann, *Application manual power semiconductors - Semikron*. ISLE Verlag Ilmenau, 2015.

Assumptions and derivations for Table 1.1

The data which has been derived in Table 1.1 is:

- The gross volumes of the Tesla Model 3, Toyota Prius IV, Chevy Bolt and Audi e-tron
- The torque and gross volume of the presented machine assuming it engineered for mass production.

The net volume of the machines presented in Table 1.1 are derived as

$$V_{net,EM} = \pi r_{\text{se}}^2 L_{\text{act}} \tag{A.1}$$

where L_{act} is the active length and r_{se} is the stator external radius of the machine. The geometrical information for the machines can be found in the references provided in Table 1.1 and for the prototyped machine is available in *Paper VII* and *Paper IX* .

The gross volume of the machines includes the end winding and the housing. The gross volume information could only be found for the BMW i3 machine, which has a gross to net volume ratio of 2.2. The values for the other machines including the production version of the machine presented are derived introducing increase factors on both the axial length and the the outer radius. To find the axial length, the increase factor is set to be a function of the winding type, in order to consider the end winding length and the distance from the end winding to the housing. Furthermore, in a conservative manner, it is assumed that an additional factor is used for the direct cooling to account for space needed to redistribute the coolant flow in the end section. The values used are presented in Table A.1.

Table A.1: Length increase factors

$k_{\text{inc,wind}}$	Distributed winding	1.8
	Hairpin winding	1.6
	Concentrated winding	1.4
$k_{\text{inc,cool,l}}$	Jacket cooling	1
	Direct cooling	1.1

The gross equivalent length can then be derived as

$$L_{\text{gross}} = L_{\text{act}} k_{\text{inc,wind}} k_{\text{inc,cool,l}}. \tag{A.2}$$

In a similar fashion the radius increase factor which accounts for the frame and the space needed within the frame for the cooling jacket are presented in Table A.2. For direct cooling the frame radial thickness can be reduced to the minimum, it only has structural function.

Table A.2: Radius increase factors

$k_{\text{inc,cool,r}}$	Jacket cooling	1.15
	Direct cooling	1.05

The gross equivalent radius can then be derived as

$$r_{\text{gross}} = r_{\text{se}} k_{\text{inc,cool,r}}. \tag{A.3}$$

Finally the gross volume can be calculated as

$$V_{\text{gross,EM}} = L_{\text{gross}} \pi r_{\text{gross}}^2. \tag{A.4}$$

Both the gross power density and gross torque density are calculated using the gross volume.

It is assumed that with a winding machine, which can be used for mass production of motors, a better copper space factor can be achieved. Therefore, mass produced motors can have higher torque density compared to a prototype (with significant margins during the manufacturing and assembly of the prototype). Hence, an increase in the wire diameter from 1.6 mm to 1.8 mm with the same

lamination is assumed. A second assumption is that the copper losses of the machine are kept constant moving to the production version, which means that the torque increase is proportional to the wire diameter increase. In fact the torque of the machine T is proportional to the current I passing in the coil conductors

$$T \propto I \propto JS_{\text{cu}} \tag{A.5}$$

where J is the current density and S_{cu} is the total copper area of the machine, meant as the copper area in one slot times the number of slots. Then

$$S_{\text{cu}} \propto d_{\text{wire}}^2 \tag{A.6}$$

where d_{wire} is the wire diameter. While copper losses

$$P_{\text{cu}} \propto \rho_{\text{cu}} J^2 S_{\text{cu}} \propto \rho_{\text{cu}} J^2 d_{\text{wire}}^2 \tag{A.7}$$

where ρ_{cu} is the copper resistivity. Hence, for constant copper losses

$$J \propto \frac{1}{d_{\text{wire}}}. \tag{A.8}$$

Finally, by substituting (A.8) and (A.6) in (A.5)

$$T \propto d_{\text{wire}} \tag{A.9}$$

which means that the total torque increase is 12.5% ($1.8/1.6 = 1.125$). However, as shown in Fig. 4.4, the machine torque is not linear with current, at high currents, because of core saturation. For this reason a 10% increase in torque for the mass-produced motor compared to the prototype is assumed instead.

LP network derivations

The thermal resistance and capacitance for the LP models presented in Chapter 5 are here derived. The materials properties used are listed in Table B.1. Table B.2 presents a list of the geometrical parameters used in the derivations. Thermal capacitance are derived by evaluating the volume of the different parts and the material specific heat and calculated as per (2.11). The values obtained are reported in Table B.3. Thermal resistance are derived as follows for the different parts of the machine. Numerical values of thermal resistance are reported in in Table B.5 for the inverter heatsink.

B.1 Direct cooling machine LP

The active winding to stator yoke thermal resistance is calculated as

$$R_{\mathrm{th,AW-sy}} = \frac{t_{\mathrm{coil}}/2}{2QL_{\mathrm{act}}h_{\mathrm{coil}}\lambda_{\mathrm{eq,w}}} + \frac{t_{\mathrm{B}}}{S_{\mathrm{B}}\lambda_{\mathrm{B}}} + R_{\mathrm{th,te}}/2 + \frac{ln\left(\frac{r_{\mathrm{s,ext}}-h_{\mathrm{sy}}/2}{r_{\mathrm{s,ext}}-h_{\mathrm{sy}}}\right)}{2\pi L_{\mathrm{act}}\lambda_{\mathrm{xy,fe}}} \tag{B.1}$$

where $\lambda_{\mathrm{eq,w}}$ is the equivalent thermal conductivity of the coil calculated as in *Paper 5* and *Paper 7* resulting in a value of 4.8 W/(m K), the teeth equivalent thermal resistance is calculated as

$$R_{\mathrm{th,te}} = \frac{h_{\mathrm{th}}}{QL_{\mathrm{act}}w_{\mathrm{th}}\lambda_{\mathrm{xy,fe}}}. \tag{B.2}$$

The active winding to coolant thermal resistance is calculated as

$$R_{\mathrm{th,AW-co}} = \frac{t_{\mathrm{coil}}/2}{2QL_{\mathrm{act}}h_{\mathrm{coil}}\lambda_{\mathrm{eq,w}}} + \frac{t_{\mathrm{pott}}}{2QL_{\mathrm{act}}h_{\mathrm{coil}}\lambda_{\mathrm{f}}} + \frac{1}{S_{\mathrm{SC}}HTC_{\mathrm{SC}}} \tag{B.3}$$

where HTC_{SC} is the heat transfer coefficient for the slot channels from Table B.4.

The end winding to coolant thermal resistance is calculated as

$$R_{\mathrm{th,EW-co}} = \frac{t_{\mathrm{coil}}/2}{0.5 S_{\mathrm{EW}} \lambda_{\mathrm{eq,w}}} + \frac{t_{\mathrm{pott}}}{S_{\mathrm{EW}} \lambda_{\mathrm{f}}} + \frac{1}{S_{\mathrm{EW}} HTC_{\mathrm{EW}}} \tag{B.4}$$

where HTC_{EW} is the heat transfer coefficient for the slot channels from Table B.4, S_{EW} is the total external surface of the end winding including the potting on the two sides of the motor (a 0.5 is added assuming that the actual end-winding is only present inside half of the external surface).

The stator yoke to coolant thermal resistance is calculated as

$$R_{\mathrm{th,sy-co}} = \frac{1}{S_{\mathrm{IC}} HTC_{\mathrm{IC}}} + \frac{\pi}{Q^2 L_{\mathrm{act}} h_{\mathrm{sy}} \lambda_{\mathrm{xy,fe}}} \tag{B.5}$$

where HTC_{IC} is the heat transfer coefficient for the iron channels from Table B.4.

The frame to coolant thermal resistance is calculated as

$$R_{\mathrm{th,fr-co}} = \frac{1}{S_{\mathrm{F}} HTC_{\mathrm{FO}}} + \frac{ln\left(\frac{r_{\mathrm{s,ext}} + t_{\mathrm{fr,DC}}/2}{r_{\mathrm{s,ext}}}\right)}{2\pi L_{\mathrm{act}} \lambda_{\mathrm{al}}} \tag{B.6}$$

where HTC_{FO} is the frame to oil heat transfer coefficient from Table B.4.

The rotor structure is simplified and modelled as in [54] using (2.13) and (2.14) The airgap thermal resistance $R_{\mathrm{th,airgap}}$ is modelled as a function of the rotor mechanical speed and air temperature as in [54] and *Paper 5*.

The thermal resistance between stator yoke and magnets $R_{\mathrm{th,st-pm}}$ is calculated as

$$R_{\mathrm{th,st-pm}} = R_{\mathrm{th,te}} + R_{\mathrm{th,airgap}} + R_{\mathrm{th,r-out}} + R_{\mathrm{th,PMpoc}} + R_{\mathrm{th,PMeq}}/2 \tag{B.7}$$

Where $R_{\mathrm{th,PMpoc}}$ is the thermal resistance due to the air pocket with thickness l_{poc} around the PM, $R_{\mathrm{th,r-out}}$ is the thermal resistance of the outer part of the rotor iron calculated with (2.14), and $R_{\mathrm{th,PMeq}}/2$ half of the equivalent PM thickness thermal resistance calculated with (2.14) considering parallel paths as in [54].

The PM to rotor yoke thermal resistance is calculated as

$$R_{\mathrm{th,pm-ry}} = R_{\mathrm{th,PMpoc}} + R_{\mathrm{th,PMeq}}/2 + R_{\mathrm{th,ry}}/2 \tag{B.8}$$

where $R_{\mathrm{th,ry}}$ is the rotor yoke equivalent thermal resistance calculated with (2.14).

The rotor yoke to bearing thermal resistance are calculated as

$$R_{\mathrm{th,ry-be}} = R_{\mathrm{th,ry}}/2 + \frac{t_{\mathrm{poc}}}{2\pi r_{\mathrm{sh}} L_{\mathrm{act}} \lambda_{\mathrm{air}}} + R_{\mathrm{th,sh}}/2 + R_{\mathrm{th,sh-bear}}/4 \tag{B.9}$$

where $R_{\mathrm{th,sh}}$ is the thermal resistance of the shaft calculated with (2.14). While the shaft to bearing are modelled as in [59, 60]

$$R_{\mathrm{th,sh-bear}} = 29.7(0.06 - r_{\mathrm{bear}}). \tag{B.10}$$

The bearing to frame thermal resistance are modelled as in [59, 60]

$$R_{\mathrm{th,bear-fr}} = R_{th,sh-bear}/4. \tag{B.11}$$

The stator yoke to frame thermal resistance is calculated as

$$R_{\mathrm{th,sy-fr}} = \frac{ln\left(\frac{r_{\mathrm{s,ext}}+t_{\mathrm{fr,DC}}/2}{r_{\mathrm{s,ext}}}\right)}{2\pi L_{\mathrm{act}}\lambda_{\mathrm{al}}} + \frac{ln\left(\frac{r_{\mathrm{s,ext}}}{r_{\mathrm{s,ext}}-h_{\mathrm{sy}}/2}\right)}{2\pi L_{\mathrm{act}}\lambda_{\mathrm{xy,fe}}} + \frac{t_{\mathrm{poc}}}{2\pi r_{\mathrm{s,ext}} L_{\mathrm{act}}\lambda_{\mathrm{air}}}. \tag{B.12}$$

The active winding to end winding thermal resistance is found as in [60] considering only the copper conducting the heat

$$R_{\mathrm{th,AW-EW}} = \frac{l_{\mathrm{av}}}{6QS_{\mathrm{Cu,slot}}\lambda_{\mathrm{w}}} \tag{B.13}$$

B.2 Cooling jacket machine LP

The thermal resistances that are calculated differently from the direct cooling machine are here listed, all the others are to be considered the same.

The active winding to stator teeth $R_{\mathrm{th,AW-te}}$ is assuming a slot liner instead of a bobbin between the teeth and the coil and is calculated as

$$R_{\mathrm{th,AW-te}} = \frac{t_{\mathrm{coil}}/2}{2QL_{\mathrm{act}}h_{\mathrm{coil}}\lambda_{\mathrm{eq,w}}} + \frac{t_{\mathrm{sl}}}{S_{\mathrm{B}}\lambda_{\mathrm{sl}}} \tag{B.14}$$

The frame to coolant $R_{\mathrm{th,sy-co}}$ is calculated as

$$R_{\mathrm{th,fr-co}} = \frac{1}{S_{\mathrm{WJ}}HTC_{\mathrm{WJ}}} \tag{B.15}$$

where HTC_{WJ} is the heat transfer coefficient for the water jacket channels from Table B.4.

The stator teeth to PM thermal resistance is calculated as

$$R_{\mathrm{th,st-pm}} = R_{\mathrm{th,te}}/2 + R_{\mathrm{th,airgap}} + R_{\mathrm{th,r-out}} + R_{\mathrm{th,PMpoc}} + R_{\mathrm{th,PMeq}}/2. \tag{B.16}$$

The stator yoke to frame thermal resistance is calculated as

$$R_{\mathrm{th,sy-fr}} = \frac{ln\left(\frac{r_{\mathrm{s,ext}}+t_{\mathrm{fr,CJ}}/2}{r_{\mathrm{s,ext}}}\right)}{2\pi L_{\mathrm{act}}\lambda_{\mathrm{al}}} + \frac{ln\left(\frac{r_{\mathrm{s,ext}}}{r_{\mathrm{s,ext}}-h_{\mathrm{sy}}/2}\right)}{2\pi L_{\mathrm{act}}\lambda_{\mathrm{xy,fe}}} + \frac{t_{\mathrm{poc}}}{2\pi r_{\mathrm{s,ext}} L_{\mathrm{act}}\lambda_{\mathrm{air}}}. \tag{B.17}$$

The internal air of the machine in the end section is modelled for the machine with the external cooling jacket. The three thermal resistances $R_{\mathrm{th,EW-fr}}$, $R_{\mathrm{th,EW-ry}}$ and $R_{\mathrm{th,ry-fr}}$ are in fact speed dependent and modelled analytically based on empirical data as in [54, 59]

Table B.1: Solid material thermal properties

Material	Property	Value	Unit
Stator and rotor Lamination	$\lambda_{\mathrm{xy,fe}}/\lambda_{\mathrm{z,fe}}$	28/1.5	W/(m K)
	C_p	486	J/(kg K)
	ρ	7700	kg/m^3
Aluminum Frame - A356 Temper-T6	λ_{al}	128	W/(m K)
	C_{p}	900	J/(kg K)
	ρ	2600	kg/m^3
Magnets - NdFeB	λ_{PM}	8	W/(m K)
	C_{p}	450	J/(kg K)
	ρ	7000	kg/m^3
Steel shaft - AISI 4340	λ_{s}	44.5	W/(m K)
	C_{p}	475	J/(kg K)
	ρ	7850	kg/m^3
Copper wire	λ_{w}	287	W/(m K)
	C_{p}	376	J/(kg K)
	ρ	8800	kg/m^3
In-slot and end-turn potting material - Epoxy	λ_{f}	1.9	W/(m K)
	C_{p}	300	J/(kg K)
	ρ	4000	kg/m^3
Bobbin material PTFE	λ_{B}	0.25	W/(m K)
	C_{p}	950	J/(kg K)
	ρ	900	kg/m^3
Slot liner	λ_{sl}	0.15	W/(m K)

Table B.2: Geometrical data used to derive the LP model

Quantity	Symbol	Value	unit
Number of slots	Q	12	-
Active machine length	L_{act}	100	mm
Average conductor length of half turn	l_{av}	140	mm
Thickness of bobbin	t_{B}	0.1	mm
Thickness of epoxy between coil and channels	t_{pott}	2	mm
Thickness of coil	t_{coil}	4.5	mm
Thickness of air pocket	t_{poc}	0.02	mm
Thickness of frame direct cooling	$t_{\text{fr,DC}}$	5	mm
Thickness of frame cooling jacket	$t_{\text{fr,CJ}}$	20	mm
Thickness slot liner	t_{sl}	0.3	mm
Stator tooth height	h_{th}	21.6	mm
Stator yoke height	h_{sy}	12.9	mm
Coil height	h_{coil}	17	mm
Stator toot width	w_{th}	17.2	mm
Average bearing radius	r_{bear}	24	mm
Average PM radius	r_{PM}	48	mm
Rotor yoke external radius	$r_{\text{ry,ext}}$	43	mm
Rotor external radius	$r_{\text{r,ext}}$	55	mm
Stator external radius	$r_{\text{s,ext}}$	90	mm
Frame external radius	$r_{\text{f,ext}}$	95	mm
Shaft radius	r_{sh}	27.5	mm
Middle of stator yoke radius	r_{my}	82	mm
Slot channels total surface	S_{SC}	0.039	m^2
End winding external wet surface	S_{EW}	0.05	m^2
Stator yoke channels total surface	S_{IC}	0.07	m^2
Jacket to water channels surface	S_{WJ}	0.023	m^2
Frame wet contact surface	S_{F}	0.07	m^2
Surface of bobbins facing the slots	S_{B}	0.08	m^2
Copper area in a slot	$S_{\text{Cu,slot}}$	0.08	m^2

Table B.3: LP thermal capacitance values

Model part	Value [J/K]
Permanent magnets	300
Winding and epoxy resin in the slot	1120
Winding and epoxy resin in the end winding	480
Stator lamination	4000
Outer rotor iron	700
Shaft and rotor yoke	3000
Bearings	170
Inverter heatsink	250
Frame direct cooling	2000
Frame cooling jacket	4000

Table B.4: Machine average convection heat transfer coefficients as a function of flow rates at a coolant temperature of 30°C, derived in *Paper V* and *Paper VII*

Model part	Flow rate [l/min]					
	2	3	4	6	8	
Jacket channels (H_2O/glycol)	4000	6300	8600	13500	18000	[W/m^2 K]
Stator yoke channels (oil)	100	127	150	200	250	[W/m^2 K]
Frame wet surface (oil)	130	174	210	270	320	[W/m^2 K]
Slot channels (oil)	150	200	240	320	400	[W/m^2 K]
EW wet surface (oil)	120	158	190	250	310	[W/m^2 K]

Table B.5: Thermal resistance inverter heatsink

Model part	Flow rate l/min					
	2	3	4	6	8	
Inverter heatsink (H_2O/glycol)	0.09	0.072	0.054	0.042	0.033	[K/W]
Inverter heatsink (oil)	0.18	0.144	0.108	0.084	0.066	[K/W]